geosciences

MDPI

Article

Seismic Activity of the Manisa Fault Zone in Western Turkey Constrained by Cosmogenic ^{36}Cl Dating

Nasim Mozafari [1,*], Çağlar Özkaymak [2,3], Dmitry Tikhomirov [1,4], Susan Ivy-Ochs [5], Vasily Alfimov [5], Hasan Sözbilir [6,7], Christian Schlüchter [1] and Naki Akçar [1]

1 Institute of Geological Sciences, University of Bern, Baltzerstrasse 1+3, 3012 Bern, Switzerland; dmitry.tikhomirov@geo.uzh.ch (D.T.); christian.schluechter@geo.unibe.ch (C.S.); akcar@geo.unibe.ch (N.A.)
2 Department of Geological Engineering, Afyon Kocatepe University, Ahmet Necdet Sezer Kampusü Gazligöl Yolu, Afyonkarahisar 03200, Turkey; caglarozkaymak@aku.edu.tr
3 Earthquake Implementation and Research Center, Afyon Kocatepe University, Afyonkarahisar 03200, Turkey
4 Department of Geography, University of Zurich, Winterthurerstrasse 190, 8057 Zürich, Switzerland
5 Institute for Particle Physics, ETH Hönggerberg, Schafmattstrasse 20, 8093 Zürich, Switzerland; ivy@phys.ethz.ch (S.I.-O.); vassili.alfimov@gmail.com (V.A.)
6 Geological Engineering Department, Dokuz Eylül University, Izmir 35160, Turkey; hasan.sozbilir@deu.edu.tr
7 Earthquake Research and Implementation Center, Dokuz Eylül University, Izmir 35160, Turkey
* Correspondence: nasim.mozafari@geo.unibe.ch

Abstract: This study reports on the cosmogenic ^{36}Cl dating of two normal fault scarps in western Turkey, that of the Manastır and Mugırtepe faults, beyond existing historical records. These faults are elements of the western Manisa Fault Zone (MFZ) in the seismically active Gediz Graben. Our modeling revealed that the Manastır fault underwent at least two surface ruptures at 3.5 ± 0.9 ka and 2.0 ± 0.5 ka, with vertical displacements of 3.3 ± 0.5 m and 3.6 ± 0.5 m, respectively. An event at 6.5 ± 1.6 ka with a vertical displacement of 2.7 ± 0.4 m was reconstructed on the Mugırtepe fault. We attribute these earthquakes to the recurring MFZ ruptures, when also the investigated faults slipped. We calculated average slip rates of 1.9 and 0.3 mm yr^{-1} for the Manastır and Mugırtepe faults, respectively.

Keywords: active tectonics; fault scarp dating; cosmogenic ^{36}Cl; Gediz Graben; western Anatolia; earthquake; Holocene

check for updates

Citation: Mozafari, N.; Özkaymak, Ç.; Tikhomirov, D.; Ivy-Ochs, S.; Alfimov, V.; Sözbilir, H.; Schlüchter, C.; Akçar, N. Seismic Activity of the Manisa Fault Zone in Western Turkey Constrained by Cosmogenic ^{36}Cl Dating. *Geosciences* **2021**, *11*, 451. https://doi.org/10.3390/geosciences11110451

Academic Editors: Rosa Nappi and Jesus Martinez-Frias

Received: 23 September 2021
Accepted: 29 October 2021
Published: 31 October 2021

Publisher's Note: MDPI stays neutral with regard to jurisdictional claims in published maps and institutional affiliations.

Copyright: © 2021 by the authors. Licensee MDPI, Basel, Switzerland. This article is an open access article distributed under the terms and conditions of the Creative Commons Attribution (CC BY) license (https://creativecommons.org/licenses/by/4.0/).

1. Introduction

Although earthquakes are one of the most hazardous natural disasters, seismic records from instrumental and historical earthquake data cover only a limited time frame [1–4]. Therefore, the forecasting of future earthquake events and disaster mitigation design are based upon short and incomplete seismic records (e.g., [1]). The dearth of such data limits our understanding of the spatial extent of deformation and magnitude of future earthquakes, which may lead to a misevaluation of high seismic risk areas [5–7].

Numerous fault studies have been conducted worldwide using different techniques (e.g., [8–14]). One of the possible tools for tracking the pace of earthquakes on individual faults over timeframes that exceed those included in the existing seismic records, is fault scarp dating. This is a valuable tool that directly date episodic exposures of normal fault scarps produced by large magnitude earthquakes and was first proposed by Zreda and Noller [15]. This tool has been used and progressively improved by many other researchers over the last two decades [15–38]. The investigation of fault scarp exposure using cosmogenic ^{36}Cl allows for the reconstruction of the timing, vertical displacement, recurrence interval, and magnitude of earthquakes as well as the fault slip rate. Thereby, the aforementioned technique offers the opportunity to extend the timeframe of slip histories on individual faults providing additional knowledge with respect to regional seismic behavior. The overall dating concept is as follows. On a fresh fault surface, exposed by

a dip-slip component of rupture, cosmogenic ^{36}Cl begins to accumulate along the newly exposed segment at a uniform distribution and at a higher rate than the unexposed part of the scarp under the colluvium. Periods of earthquake activity are then disentangled based on: (1) cosmogenic ^{36}Cl concentrations measured along a continuous strip on the fault scarp; and (2) differences in ^{36}Cl accumulation rates on the exposed and covered surfaces during the quiescence times [15–19,33].

Strong earthquakes in extensional tectonic regimes may cause surface ruptures and deformation, principally documented as normal fault scarps that juxtapose Quaternary alluvium or colluvium against bedrock at a variety of scales [39,40]. An example of such a setting is Western Anatolia, Turkey, which includes approximately E-W-trending graben systems as a result of roughly N-S extension evidenced by the occurrence of large normal fault scarps occurring in the limestone bedrock (Figure 1).

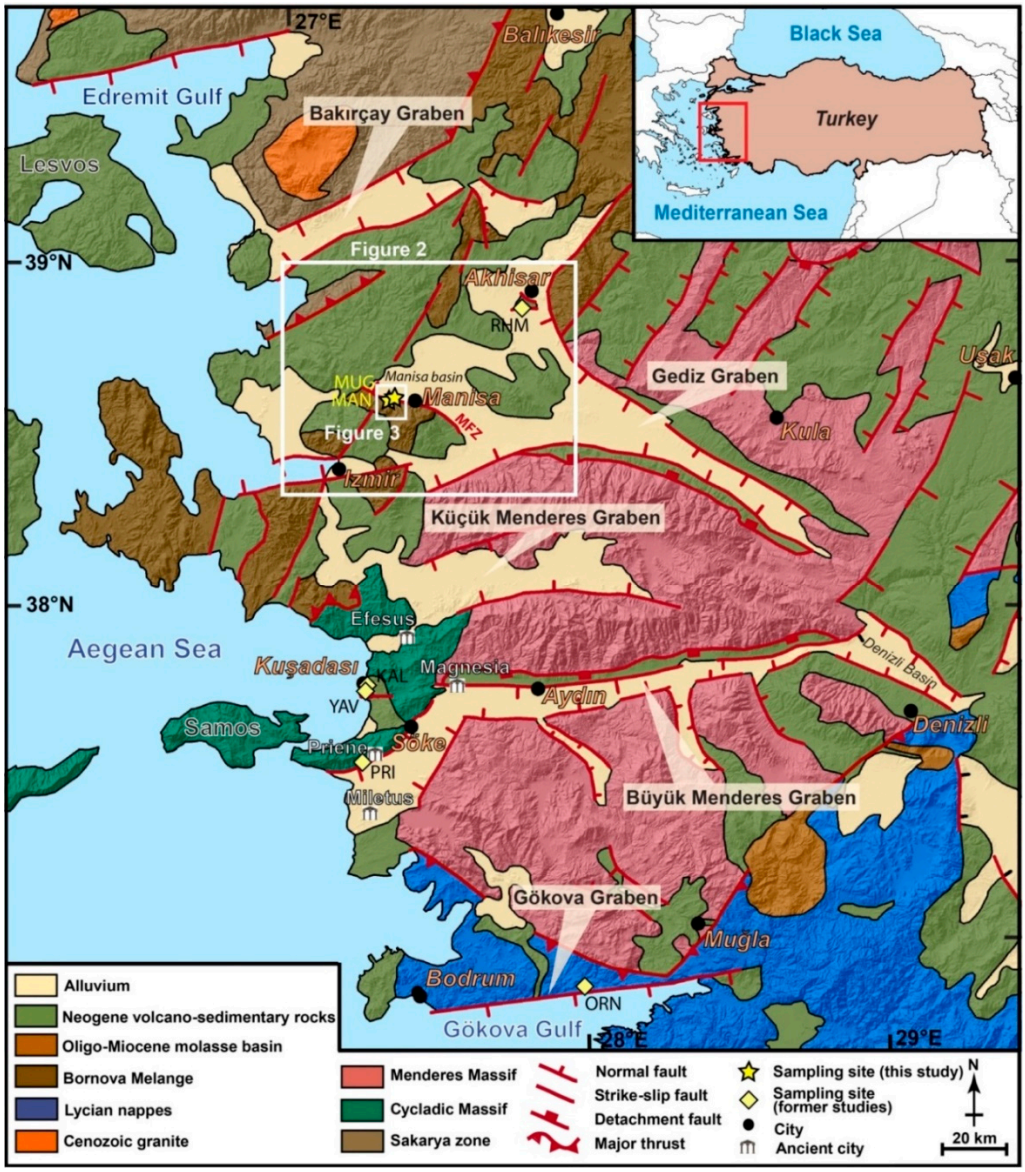

Figure 1. Simplified geological map of western Anatolia showing major structural elements and location of Manastır and Mugırtepe faults (modified from [24,33,34,41,42]). Inset white boxes mark the location of the Figures 2 and 3. Faults abbreviations: MFZ: Manisa Fault Zone, RHM: Rahmiye, MAN: Manastır, MUG: Mugırtepe, KAL: Kalafat, YAV: Yavansu, PRI: Priene-Sazlı, ORN: Ören.

In addition, the active zone of the Izmir-Balıkesir Transfer Zone (IBTZ) extended between Izmir and Balıkesir cities, generally consists of N-S and NNE-SSE trending strike slip faults, and acts as the western border of the E-W-trending grabens i.e., Gediz (Figure 1). IBTZ was demonstrated to be a deep crustal transform fault zone during Late Cretaceous, which acted as a transtensional transfer zone in the Neogene period ([43–45]). Recent seismicity with focal mechanism, Global Navigation Satellite System (GNSS) measurements and several geological studies indicate that IBTZ is undergoing an E-W shortening as well as N-S extension (e.g., [43,44,46–49]). Here, recent investigations confirm a very close connection between the normal surface ruptures and large magnitude 6 or higher earthquakes (e.g., [33–35,50–52]). Earthquakes are considered imminent in this intensively active region, with the most recent destructive event occurring offshore Samos Island (south of Izmir region) on 30th October 2020, with Mw 7.0 [53]. However, the association of historic earthquakes with individual normal faults in Western Anatolia continues to be very limited (e.g., [54–56]).

In this study, we focus on one of the fault zones in the western sector of the Gediz Graben (western Turkey) to obtain a broader insight into the seismic behavior of active faults beyond the historical and instrumental earthquake archives (Figure 2). We focus on two fault scarps within the western part of the Manisa Fault Zone (MFZ), documented as one of the most seismically-damaged regions in history [3,48,55,57,58]. Specifically, we applied the Fault Scarp Dating Tool (FSDT) computation code [37] to recover rupture histories of the Manastır and Mugırtepe faults (MAN and MUG in Figure 3, respectively) in the western segment of the active MFZ. We analyzed 87 samples from the Manastır fault surface and remodeled the cosmogenic ^{36}Cl concentrations already measured on the Mugırtepe fault surface [24]. We show that the MFZ experienced numerous ground-rupturing earthquakes during Holocene. We also provide a comparison and interpretation of our results with respect to paleoseismological data in our effort to better constrain the seismic history for the western MFZ. We find that this region experienced clustered earthquakes during late Holocene.

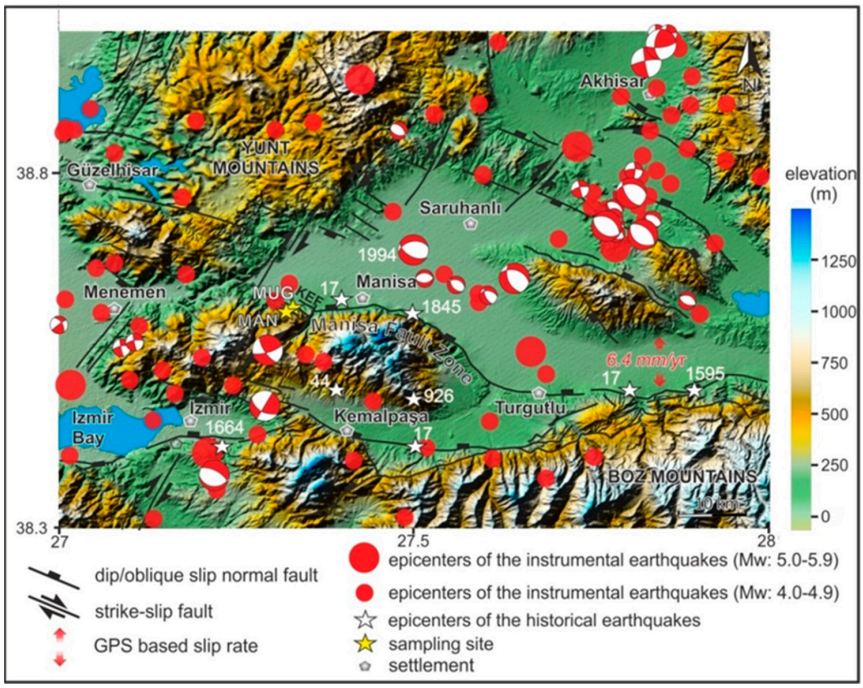

Figure 2. Seismotectonic map of the Izmir-Manisa region showing the epicenters of instrumental and historical earthquakes (modified from [59]). MAN: Manastır fault, MUG: Mugırtepe fault, KEF: Keçiliköy fault; GPS based slip rate is from [47].

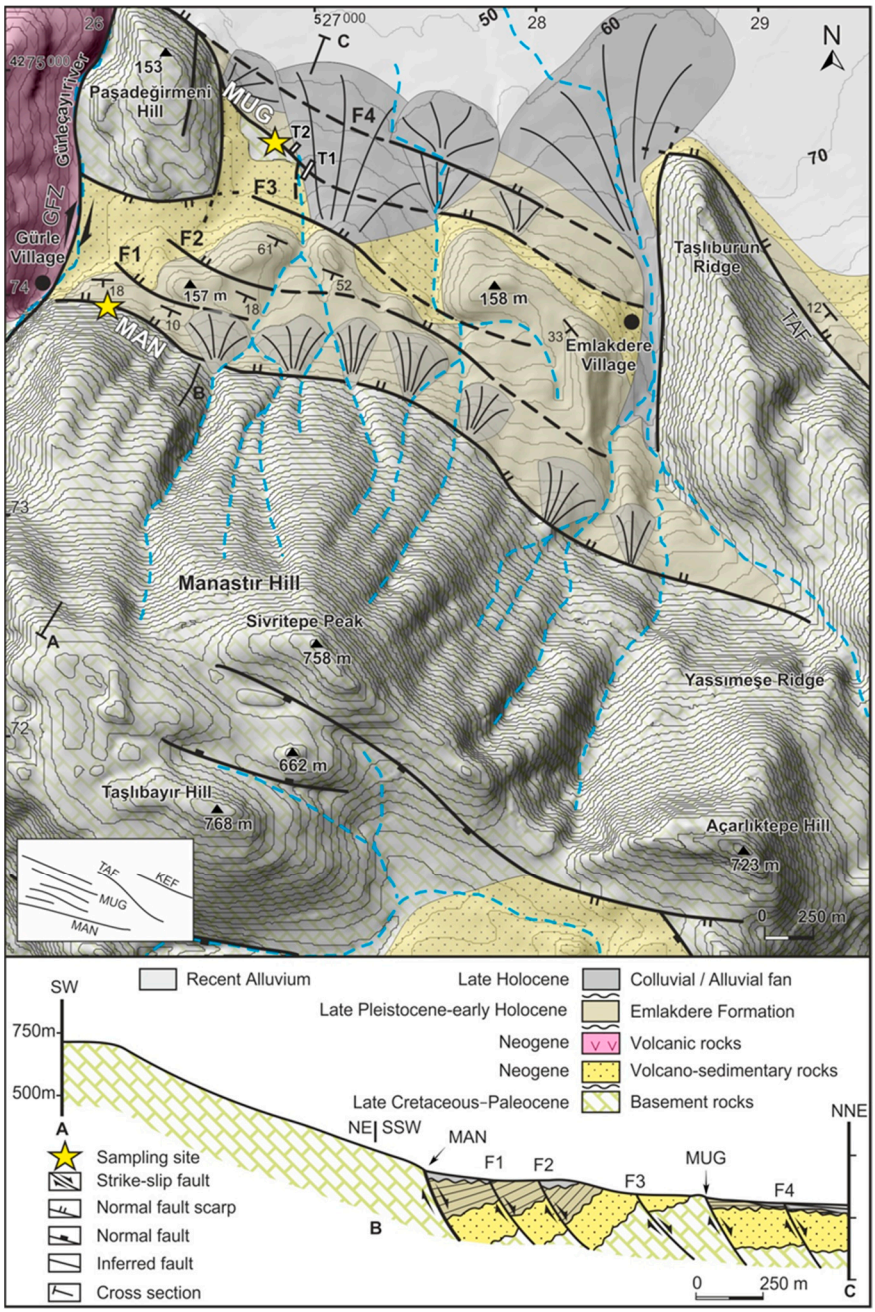

Figure 3. Detailed geological map of the study area showing NW–SE-trending active faults; location of paleoseismological trench sites from [59] along Mugırtepe fault are shown as T1 and T2. Yellow stars locate fault scarp dating sampling sites of Manastır (MAN) and Mugırtepe (MUG) faults, respectively. GFZ: Gürle Fault Zone, TAF: Taşlıburun fault, KEF: Keçiliköy fault; Inset is a simple sketch to show Taşlıburun fault, which its location is beyond the map frame. Geological cross section shows stratigraphic and structural relationships of the units. Note that offset of Quaternary deposits by several instances of synthetic Holocene faulting in the hangingwall of the Manastır fault is the most direct evidence for their activity (modified from [24,59]).

2. Study Area

The approximately WNW-ESE-trending MFZ within the Gediz Graben extends for 35 km at the southern margin of the Manisa Basin [44,51,60] and includes a large number of Quaternary fault scarps [41,44,51,61,62] (Figures 1 and 2). The MFZ is considered to be a northeastward-arcuate structure of the graben [59]. Different groups of kinematic indicators, including sinistral strike-slip, dextral strike-slip, and normal-slip denote three phases

of activity in the MFZ since the early Miocene, respectively [44,51]. In the investigated area (westernmost part of the MFZ), at least six WNW-ESE-trending and NNE-dipping normal fault scarps displaced Late Cretaceous–Paleocene carbonate footwall, against the Late Pleistocene–early Holocene sediments of Emlakdere Formation, occasionally covered by colluvium deposits on the hangingwall (Figures 3 and 4). This group of faults comprise the Manastır, F1, F2, F3, Mugırtepe, and F4 form separate scarp terraces and defines the southwestern boundary of the Manisa Basin. The Manastır fault was probably initiated as a master fault with the onset of graben system formation during the Early-Miocene or later in western Anatolia. While the other faults are interpreted to be formed as a consequence of basinward migration evidenced by back-tilting of the Emlakdere Formation and the Neogene volcano-sedimentary rocks [59]. The strata are parallel in these rock units separated by unconformity, indicating synchronized tilting [59] (Figures 3 and 4). Gradual deposition and rotation of hangingwall deposits caused by slip on the Manastır master fault is evidenced by a clear angular unconformity recorded in the upper part of the Emlakdere Formation showing dissimilar dip of strata of similar lithology. Based on the radiocarbon ages, this syn-depositional tilting was considered to occur between ca. 19 and 9 cal kyr BP [59]. In an extensional tectonic setting, shallow antithetic and synthetic faults within the hangingwall of the larger master fault are typically prevalent; these parallel/subparallel faults are refractions of the master fault dip and maintain evolution towards the basin and can move in synchrony with the master fault they are linked to (e.g., [63–65]). Secondary faults are normally incapable of producing significant earthquakes with magnitudes exceeding 5.5 and are considered as non-seismogenic faults [64]. Among this set of faults, the approximately 4.5-km long and 140-m-high Manastır fault is considered as the master fault. The Manastır fault is connected to the approximately 3-km long Taşlıburun fault through an N-S-trending relay ramp (Figure 3). The Taşlıburun fault is, in turn, linked to the Keçiliköy fault with a similar length on its northeast side (Figures 2 and 3). These three faults constitute an en échelon structure linked to MFZ at its westernmost end [44].

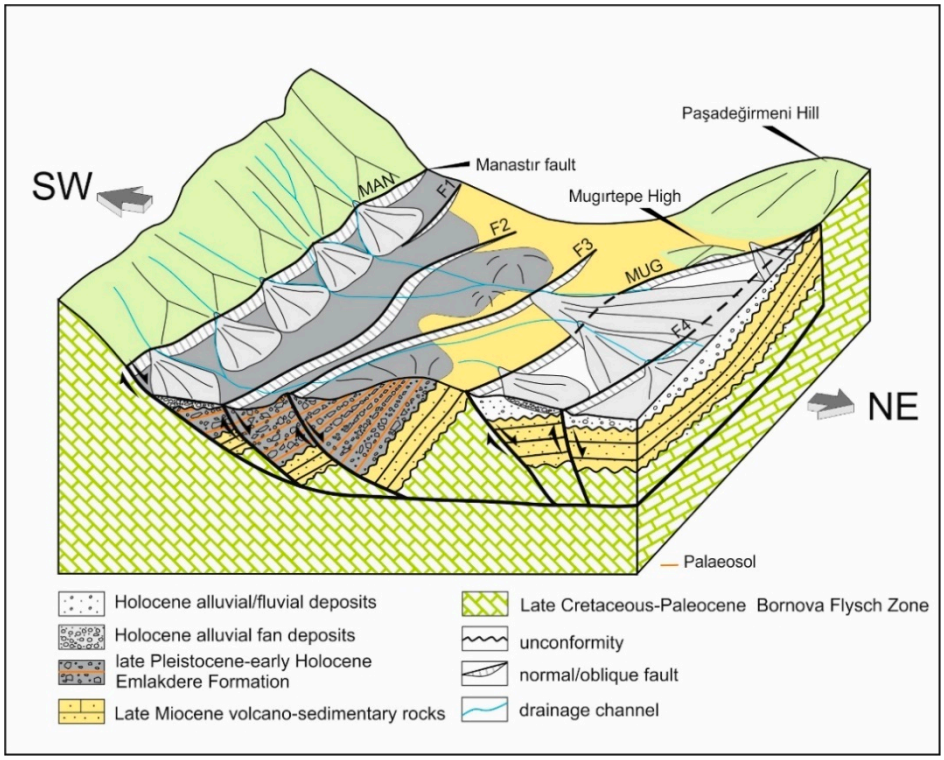

Figure 4. 3D view of western Manisa Fault Zone showing the staircase of fault scarps in the Manastır hangingwall. MAN: Manastır, MUG: Mugırtepe. Note that in the cartoons the exact horizontal and vertical scales, vertical displacement values as well as thickness of sedimentary layers are disregarded. However, MAN fault depth is known to be 5–10 km in about 10 km northeast of Manisa.

The Manastır fault activity is expressed by sets of screes, landslides, and at least two generations of triangular facets [59]. The overprinting of the strike-slip slickenlines by the dip-slip ones indicate reactivation of the Manastır fault. Accordingly, the exposure of the sampled fault surface is attributed to an approximately N-S trending extensional tectonic regime that started in Quaternary. The Manastır fault extends to the NE side of Manastır Hill and intersects the NW end of the approximately 1.5 km wide strike-slip Gürle Fault Zone [59] (Figure 3). Gürle Fault Zone, a segment of IBTZ, is characterized by segmented parallel-subparallel faults, which extends to the north of Paşadeğirmeni Hill and bounds MFZ on its west end. All the synthetic faults located at the western part of the MFZ are assumed to be linked in depth to the master Manastır fault and there are five secondary faults to the north (F1, F2, F3, Mugırtepe, and F4), which run parallel to the Manastır fault [59]. Faults F1, F2, and F3 are approximately 1, 3, and 2 km in length, respectively. Their dip ranges between 45° and 65° NNE with an average scarp height of 3 m, whereas the Mugırtepe fault has a maximum of 4 m height and is approximately 3 km long. To the northwest, the Mugırtepe and the similar-sized F4 faults merge at the foot of Paşadeğirmeni Hill and cut across the Gürle Fault Zone [59] (Figure 3).

Six strong earthquakes have been recorded in Manisa and the surrounding region historically (Figure 2). The oldest occurred in Lydia in 17 AD and had an intensity of IX. It caused significant damage in 13 or 16 ancient cities, mostly located in the Manisa Basin [1,48,55,57,58]. This earthquake is an example of the discrepancies in the geographic locations and intensity/magnitudes of ancient earthquakes recorded by different sources. The succeeding destructive earthquake dates back to 44 AD and likely damaged the ancient Greek cities of Magnesia, Samos, Militus and Ephesus, with an intensity of VIII [1,3,58,66]. In addition, [1] reported an earthquake in 926 (925) AD, in the province of the Thraceseans, caused traverse of the region by the Gediz and Menderes rivers. An earthquake in 1595 was documented ca. 60 km to the east of Manisa [1,55,67]. Another major earthquake with an intensity of VII was reported to have occurred in Izmir in 1664 [1,3,66,67], although [55] claim this event to have occurred near Izmir, and perhaps towards Manisa. The last recorded historical earthquake occurred in 1845 in Lesvos, and felt in Manisa [3,66], with a reconstructed intensity of VIII [3] or M = 6.7 [68]. The earthquake of 28th January 1994, with Mw 5.2 or 5.4, is the largest instrumental earthquake recorded close to Manisa with estimated focal depth of 5 to 10 km [48,53,69] and epicentered about ten kilometers northeast of Manisa (Figure 2).

The rupture history of the Mugırtepe fault is reconstructed [24] using a Matlab® code developed by Schlagenhauf et al. [22]. They proposed two scenarios. The first one yielded two seismic events at 13.7 ± 0.8 ka and 7.8 ± 0.5 ka with a displacement of 0.5 ± 0.2 m and 2.15 ± 0.35 m, respectively. The second scenario resulted in a single seismic event of 8.5 ± 0.6 ka with a vertical displacement of 2.65 ± 0.35 m. Here, we note that this event, similar to most of the events recovered by FSDT, consists of clusters of earthquakes that occurred close in time. In addition to the abovementioned documented and reconstructed earthquakes, three palaeoearthquakes defined during the last 1 kyr using radiocarbon dating of palaeosol samples collected inside two paleoseismic trenches dug across the Mugırtepe fault [59]. These three events were tentatively linked to the historical earthquakes of 926 AD, 1595/1664 AD, and 1845 AD.

3. Materials and Methods

3.1. Sampling

To select appropriate sampling sites, we explored the fault surfaces in several outcrops along the MFZ. We considered the most suitable site as the well-preserved surface with negligible evidence of weathering (Figure 3). The site is close to the Mugırtepe fault scarp studied [24,59]. The scarp of the Manastır fault was sampled in summer 2008 following a similar sampling strategy by Mitchell et al. [16] (Figure 5). Two parallel vertical slots spaced approximately 12 cm apart were cut to a depth of 3–4 cm into the scarp surface using a hand-held circular saw with a diamond blade. The rock strip was then divided

into 5–10-cm slabs perpendicular to the vertical slots. Finally, the sample slabs were broken off with a chisel and hammer. Being vital factors for earthquake modeling, the scarp geometry elements including scarp dip, scarp height, top surface dip, and colluvium dip were determined in the field. Rock density and water content of the bedrock and colluvium were also estimated, and colluvium density was measured in the field. In addition, top and bottom positions of each sample were documented for modeling.

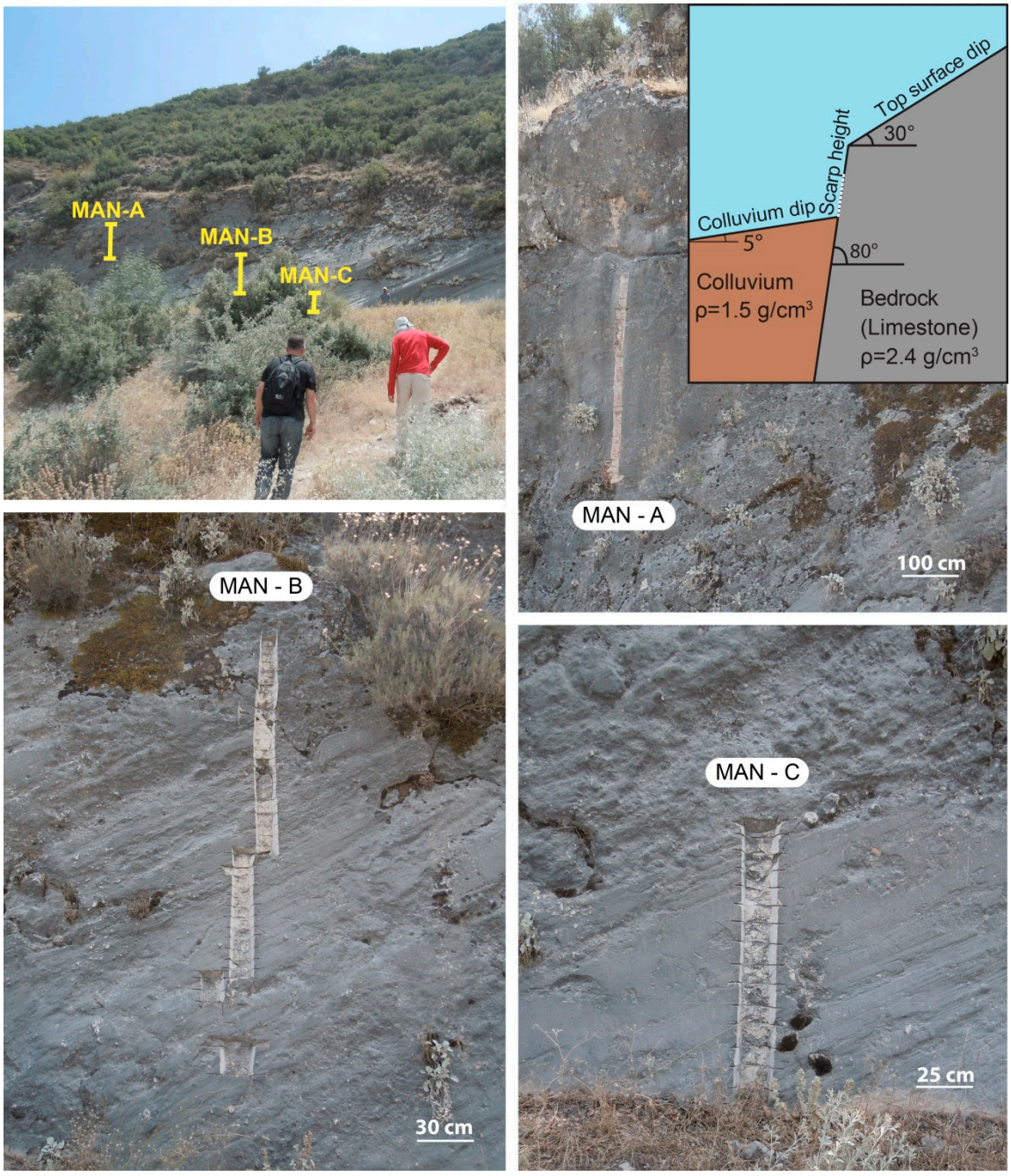

Figure 5. Manastır fault scarp, view towards SSW with three sampling strips of MAN-A, MAN-B and MAN-C. Note: lowest notch below MAN-B strip is not related to this study; Schematic sketch shows fault scarp with used parameters for modeling. White dashed line represents the sampled surface.

Along the Manastır fault scarp, three sampling strips (MAN-A, MAN-B, and MAN-C) that were spaced a few meters apart, were cut to cover the maximum height along the scarp surface (Figure 5). We collected 87 samples, which covered approximately 7 m of

the 12-m scarp surface height from the ground level; 36 samples were obtained from both MAN-A and MAN-B, and 15 samples from MAN-C. In addition, the fault scarp geometry parameters (i.e., scarp dip, scarp height, top surface dip, and colluvium dip, Figure 5) were precisely measured in the field (e.g., [22,27,37]. In comparison, Akçar et al. [24] collected 44 samples along a ca. 2.7-m sampling profile of the 4-m high Mugırtepe fault scarp (Figure 6).

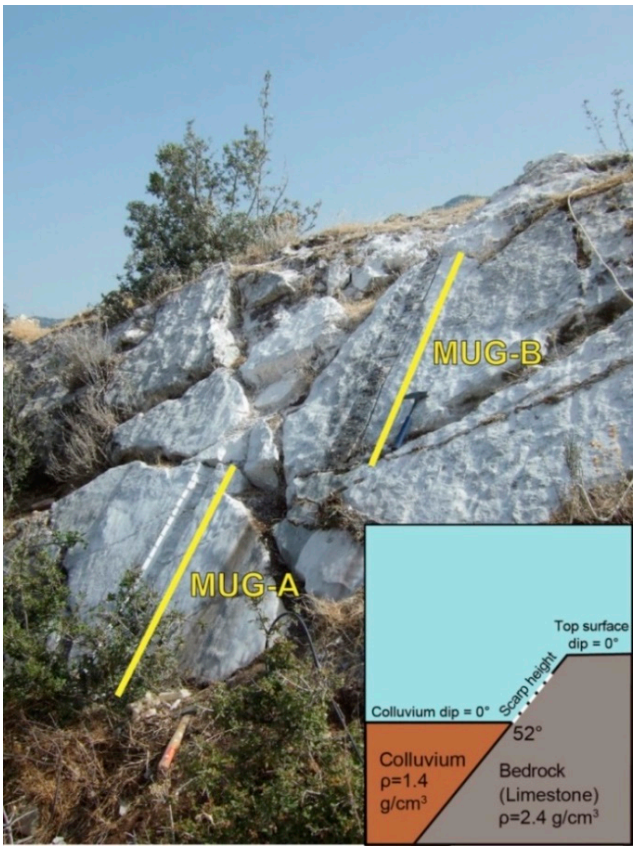

Figure 6. Mugırtepe fault scarp, view towards south with two sampling strips of MUG-A and MUG-B. The sampling has been done by [24]. Schematic sketch shows fault scarp with used parameters for modeling. White dashed line represents the sampled surface.

3.2. Cosmogenic ^{36}Cl Analysis

The samples collected from the Manastır fault were processed at the Surface Exposure Laboratory of the Institute of Geological Sciences, University of Bern, following the procedure reported by Stone et al. [70] and Ivy-Ochs et al. [71,72], and the isotope dilution method [72,73]. A full description of the standard protocol of the laboratory for ^{36}Cl extraction from limestone samples is presented in previous publications (cf. [24,33,34]). The total Cl and ^{36}Cl of the Manastır samples were measured at the TANDEM accelerator mass spectrometry (AMS) facility at ETH Zurich. The calcium concentrations of individual samples from Manastır as well as major and trace elements of five proxy samples were also measured using inductively coupled plasma mass spectrometry (ICP-MS) at SGS Mineral Services, Canada. In addition, we determined the calcium concentrations of the Mugırtepe fault scarp from the study conducted by Akçar et al. [24].

3.3. Fault Scarp Dating Tool

To analyze the distribution of ^{36}Cl concentrations accumulated on the Manastır fault scarp (MAN) and reanalyze the dataset for the Mugırtepe fault scarp (MUG), we applied the computation code based on the Monte-Carlo method, which allows the reconstructions of the time-slip histories of normal fault scarps through two separate stages of database

building and data simulation [37]. In the database-building stage, the chemical composition of the bedrock, sample positions, shielding of the scarp and colluvium are considered to calculate the production of the isotope in every sample depending on fixed slip step and rock erosion. Creation of the database improves time efficiency via the approximation of pre-calculated isotope production during each round of simulation. The maximal erosion rate was set to 15 cm kyr^{-1} to provide some flexibility in the current analysis. In the simulation stage, exposure histories are generated within an earthquake scenario based on the number of earthquakes, earthquake ages, slip values, and erosion rates (cf. [33,34]). Simulated ^{36}Cl concentration of the samples are statistically compared with measured concentrations taking into account the measurement errors of ^{36}Cl, parent elements and production rates (Tables 1–4). Following the preliminary simulation of the fault dataset, we began our main simulations by entering an excessive number of earthquakes. After identifying the most accurate number of events in terms of the lowest statistical criteria, we modeled the time-slip histories using minimum 100,000 simulations to achieve the best fit scenario based on one and two earthquake scenarios for the Manastır fault and one to three earthquake scenarios for the Mugırtepe fault. In the FSDT code [37] "Beginning of exposure" indicates the time when the ^{36}Cl starts to accumulate in the analyzed section of the fault scarp at depth, but it does not refer to any exposure and/or any seismic event. Thus, the analyzed strip is assumed to be still underground (e.g., covered by the colluvium) at the beginning of cosmogenic ^{36}Cl accumulation. The thickness of the overburden can theoretically be in the order of several meters. To avoid any confusion, in this paper we use the term "beginning of accumulation". It is important to note that the fault scarp dating process only allows for the detection of large earthquakes with considerable displacement values, thereby yielding a lower estimate of earthquake frequency (cf. [20,21,33,34]). Furthermore, episodic earthquakes occurring within the uncertainty of the analysis are not identified as a series of earthquakes but rather as a single event, which cannot be disentangled by any code. This causes lower resolution of the older ages and larger slips [37]. The simulation output is given as a plot of measured ^{36}Cl concentrations against the sample height along the sampled profile. Following a comparison of the measured and modeled ^{36}Cl concentrations, the most realistic scenario is selected based on the lowest statistic criteria.

Table 1. Input parameters of the Manastır and Mugırtepe fault scarps for earthquake modeling.

	Manastır Fault	**Mugırtepe Fault**
Latitude	38° 36.729′ N	38° 37.101′ N
Longitude	27° 17.917′ E	27° 18.498′ E
Altitude	141 m	80 m
Scarp strike	N88° E	N65° W
Colluvium dip	5°	0°
Scarp dip	80°	52°
Top surface dip	30°	0°
Scarp height	1200 cm	415 cm
Scarp rock density	2.4 g/cm^3	2.4 g/cm^3
Colluvium density	1.5 g/cm^3	1.4 g/cm^3
Rock water content	0.1%	0.1%
Colluvium water content	1%	1%
Spallation on Ca: 48.8 ± 3.5 at g^{-1} yr^{-1} [70]		
Spallation on K of 170 ± 25 at g^{-1} yr^{-1} [74]		
Spallation on Ti of 13 ± 3 at g^{-1} yr^{-1} [75]		
Spallation on Fe of 1.9 ± 0.2 at g^{-1} yr^{-1} [76]		
Epithermal neutrons from fast neutrons: 760 ± 150 n/g^{-1} yr^{-1} [77]		
Scaling scheme [78]		

Table 2. Cosmogenic nuclide data of the Manastır Fault scarp.

Sample Name	Top Position (cm)	Bottom Position (cm)	Thickness (cm)	^{36}Cl * (105 at/g)	^{36}Cl Uncertainty * (105 at/g)	Cl Total * (ppm)	Cl Total Uncertainty * (ppm)	Ca † (ppm)	O (%)	C (%)
MAN-A02	645	638	2.0	1.056	0.099	9.3	0.09	372,143	48.78	11.16
MAN-A03	638	631	2.0	1.114	0.046	9.9	0.10	346,429	52.13	10.39
MAN-A04	631	624	2.0	1.086	0.054	7.9	0.08	386,429	46.93	11.59
MAN-A05	624	617	2.0	1.056	0.045	11.2	0.11	372,143	48.78	11.16
MAN-A06	617	610	2.0	1.144	0.049	10.6	0.11	375,714	48.32	11.27
MAN-A07	610	603	3.0	1.154	0.055	9.3	0.09	346,429	52.13	10.39
MAN-A09	596	589	2.0	0.934	0.043	9.2	0.09	346,429	52.13	10.39
MAN-A10	589	582	2.0	0.905	0.048	10.6	0.11	373,571	48.60	11.21
MAN-A11	582	575	2.0	1.021	0.056	9.7	0.10	346,429	52.13	10.39
MAN-A12	575	568	2.0	1.055	0.044	9.5	0.09	373,571	48.60	11.21
MAN-A13	568	561	3.0	0.974	0.043	7.2	0.07	368,571	49.25	11.06
MAN-A14	561	554	2.0	0.840	0.037	5.4	0.05	362,143	50.08	10.86
MAN-A15	554	547	3.0	1.005	0.052	7.9	0.08	350,714	51.57	10.52
MAN-A16	547	540	2.0	0.880	0.040	8.3	0.08	370,000	49.06	11.10
MAN-A17	540	533	2.0	0.782	0.038	6.8	0.07	346,429	52.13	10.39
MAN-A18	533	526	2.0	0.827	0.036	5.7	0.06	346,429	52.13	10.39
MAN-A19	526	519	2.0	0.769	0.034	3.9	0.04	346,429	52.13	10.39
MAN-A20	519	512	2.0	1.053	0.054	5.9	0.06	360,714	50.27	10.82
MAN-A21	512	505	2.0	0.843	0.037	4.9	0.05	346,429	52.13	10.39
MAN-A22	505	498	2.0	0.796	0.042	10.7	0.11	346,429	52.13	10.39
MAN-A23	498	491	2.0	0.749	0.047	8.2	0.08	346,429	52.13	10.39
MAN-A24	491	484	3.0	0.871	0.054	8.7	0.09	346,429	52.13	10.39
MAN-A25	484	477	2.0	0.815	0.040	7.9	0.08	346,429	52.13	10.39
MAN-A26	477	470	2.0	0.774	0.039	8.4	0.08	346,429	52.13	10.39
MAN-A27	470	463	2.0	0.792	0.037	9.8	0.10	346,429	52.13	10.39
MAN-A28	463	456	2.0	0.854	0.071	10.2	0.10	369,286	49.16	11.08
MAN-A29	456	449	2.0	0.781	0.038	11.7	0.12	341,429	52.78	10.24
MAN-A30	449	442	2.0	0.747	0.035	10.0	0.10	345,000	52.31	10.35
MAN-A31	442	435	2.0	0.721	0.038	9.4	0.09	370,714	48.97	11.12
MAN-A32	435	428	2.0	0.795	0.042	10.0	0.10	354,286	51.11	10.63
MAN-A33	428	421	2.0	0.694	0.036	8.9	0.09	353,571	51.20	10.61
MAN-A35	414	407	2.0	0.800	0.045	13.5	0.13	317,857	55.84	9.54
MAN-A36	407	400	2.0	0.713	0.038	25.1	0.25	321,429	55.38	9.64
MAN-A37	400	393	2.0	0.696	0.035	21.5	0.21	320,000	55.56	9.60
MAN-A38	393	386	2.0	0.654	0.045	30.8	0.31	298,571	58.35	8.96
MAN-A39	386	379	2.0	0.565	0.031	13.2	0.13	337,143	53.33	10.11
MAN-B01	379	372	3.0	0.777	0.047	10.7	0.05	345,000	52.31	10.35
MAN-B02	372	365.5	2.0	0.694	0.033	4.8	0.11	345,000	52.31	10.35
MAN-B03	365.5	357.5	2.0	0.714	0.038	11.3	0.13	338,571	53.15	10.16
MAN-B04	357.5	351	2.0	0.791	0.046	13.3	0.08	343,571	52.50	10.31
MAN-B05	351	343	2.0	0.604	0.033	7.6	0.07	347,143	52.03	10.41
MAN-B06	343	336.5	2.0	0.582	0.034	6.9	0.06	357,143	50.73	10.71
MAN-B07	336.5	329.5	2.0	0.752	0.045	5.9	0.12	325,000	54.91	9.75
MAN-B08	329.5	322	2.0	0.740	0.045	11.8	0.23	315,714	56.12	9.47
MAN-B09	322	314	2.0	0.664	0.040	23.1	0.18	315,714	56.12	9.47
MAN-B10	314	306	2.0	0.758	0.067	17.9	0.25	323,571	55.10	9.71
MAN-B11	306	298	2.0	0.504	0.036	25.2	0.21	317,857	55.84	9.54
MAN-B12	298	290.5	2.0	0.539	0.029	21.3	0.13	333,571	53.80	10.01
MAN-B13	305.5	296.5	2.0	0.572	0.031	13.1	0.09	341,429	52.78	10.24
MAN-B14	296.5	289.5	2.0	0.663	0.058	9.1	0.09	350,000	51.66	10.50
MAN-B15	289.5	282.5	2.0	0.516	0.029	8.7	0.08	325,000	54.91	9.75
MAN-B16	282.5	277.0	2.0	0.539	0.035	7.5	0.05	364,286	49.81	10.93
MAN-B17	277.0	270.0	2.0	0.659	0.055	4.9	0.10	352,143	51.38	10.56
MAN-B18	270.0	263.5	2.0	0.578	0.032	9.5	0.08	357,143	50.73	10.71
MAN-B19	263.5	257.5	2.0	0.596	0.033	8.0	0.10	346,429	52.13	10.39
MAN-B20	257.5	252.0	2.0	0.589	0.032	10.4	0.10	346,429	52.13	10.39
MAN-B21	252.0	230.0	2.0	0.614	0.042	10.2	0.10	349,286	51.76	10.48
MAN-B24	230.0	223.0	2.0	0.529	0.029	10.1	0.15	330,714	54.17	9.92
MAN-B25	223.0	216.0	2.0	0.546	0.045	15.4	0.12	350,714	51.57	10.52
MAN-B26	216.0	207.5	2.0	0.456	0.028	12.3	0.18	335,714	53.52	10.07
MAN-B27	207.5	201.0	2.0	0.499	0.029	17.7	0.14	324,286	55.00	9.73
MAN-B28	201.0	194.0	2.0	0.601	0.033	14.1	0.14	328,571	54.45	9.86

Table 2. *Cont.*

Sample Name	Top Position (cm)	Bottom Position (cm)	Thickness (cm)	^{36}Cl * (105 at/g)	^{36}Cl Uncertainty * (105 at/g)	Cl Total * (ppm)	Cl Total Uncertainty * (ppm)	Ca † (ppm)	O (%)	C (%)
MAN-B29	194.0	187.5	2.0	0.557	0.068	14.4	0.09	342,857	52.59	10.29
MAN-B30	187.5	180.5	2.0	0.483	0.028	9.3	0.08	353,571	51.20	10.61
MAN-B31	180.5	173.5	2.0	0.515	0.028	8.2	0.06	358,571	50.55	10.76
MAN-B32	173.5	166.5	2.0	0.713	0.071	6.1	0.11	343,571	52.50	10.31
MAN-B33	166.5	160.5	2.0	0.584	0.031	11.4	0.07	356,429	50.83	10.69
MAN-B34	160.5	153.0	2.0	0.497	0.026	7.0	0.03	378,571	47.95	11.36
MAN-B35	153.0	141.0	2.0	0.574	0.042	2.8	0.04	369,286	49.16	11.08
MAN-B37	141.0	135.0	2.0	0.612	0.053	4.2	0.09	342,143	52.68	10.26
MAN-B38	135.0	127.5	2.0	0.549	0.028	8.8	0.06	371,429	48.88	11.14
MAN-B39	127.5	120.0	2.0	0.498	0.027	6.1	0.08	365,000	49.71	10.95
MAN-C01	105.0	101.0	2.0	0.535	0.030	8.4	0.08	346,429	52.13	10.39
MAN-C02	101.0	94.0	2.0	0.739	0.047	4.3	0.04	357,143	50.73	10.71
MAN-C03	94.0	88.0	2.0	0.577	0.034	6.3	0.06	364,286	49.81	10.93
MAN-C04	88.0	81.0	2.0	0.515	0.039	12.5	0.12	344,286	52.40	10.33
MAN-C05	81.0	74.3	2.0	0.555	0.041	12.4	0.12	336,429	53.43	10.09
MAN-C06	74.3	67.5	2.0	0.245	0.020	6.7	0.07	346,429	52.13	10.39
MAN-C07	67.5	60.0	2.0	0.534	0.034	10.5	0.11	338,571	53.15	10.16
MAN-C08	60.0	52.0	2.0	0.540	0.043	5.4	0.05	368,571	49.25	11.06
MAN-C09	52.0	45.0	2.0	0.557	0.042	4.3	0.04	358,571	50.55	10.76
MAN-C10	45.0	36.5	2.0	0.544	0.044	9.1	0.09	354,286	51.11	10.63
MAN-C11	36.5	30.0	2.0	0.381	0.030	10.4	0.10	357,143	50.73	10.71
MAN-C12	30.0	21.0	2.0	0.511	0.035	12.1	0.12	355,000	51.01	10.65
MAN-C13	21.0	14.0	2.0	0.402	0.030	22.1	0.22	313,571	56.40	9.41
MAN-C14	14.0	6.5	2.0	0.399	0.033	26.0	0.26	297,143	58.53	8.91
MAN-C15	6.5	0.0	2.0	0.523	0.033	27.6	0.28	296,429	58.62	8.89

* Measured with accelerator mass spectrometry (AMS). † Measured with inductively coupled plasma mass spectrometry (ICP-MS).

Table 3. Cosmogenic nuclide data of the Mugırtepe scarp [24].

Sample Name	Top Position (cm)	Bottom Position (cm)	Thickness (cm)	^{36}Cl * (105 at/g)	^{36}Cl Uncertainty * (105 at/g)	Cl Total * (ppm)	Cl Total Uncertainty * (ppm)	Ca † (ppm)	O (%)	C (%)
MUG-B01	267.5	262.5	2.0	4.512	0.125	12.5	0.12	383,571	49.69	11.51
MUG-B02	262.5	257.5	2.0	4.743	0.120	14.9	0.15	390,714	48.76	11.72
MUG-B03	257.5	250.0	2.0	4.245	0.321	14.2	0.14	382,143	49.88	11.46
MUG-B04	250.0	240.0	2.0	3.986	0.089	13.7	0.14	374,286	50.90	11.23
MUG-B05	240.0	231.5	2.0	4.127	0.121	14.0	0.14	389,286	48.95	11.68
MUG-B06	231.5	226.0	2.0	4.121	0.088	13.0	0.13	352,857	53.68	10.59
MUG-B07	226.0	218.5	2.0	4.372	0.128	17.4	0.17	389,286	48.95	11.68
MUG-B08	218.5	210.0	2.0	4.114	0.104	11.0	0.11	400,000	47.55	12.00
MUG-B09	210.0	203.5	2.0	3.808	0.108	17.3	0.17	396,429	48.02	11.89
MUG-B10	203.5	196.5	2.0	3.649	0.133	16.6	0.17	383,571	49.69	11.51
MUG-B11	196.5	189.0	2.0	3.695	0.116	17.6	0.18	396,429	48.02	11.89
MUG-B12	189.0	181.5	2.0	3.626	0.125	14.0	0.14	396,429	48.02	11.89
MUG-B13	181.5	174.5	2.0	3.309	0.124	13.9	0.14	384286	49.60	11.53
MUG-B14	174.5	166.0	2.0	3.405	0.100	16.2	0.16	384,286	49.60	11.53
MUG-B15	166.0	157.0	2.0	3.328	0.125	17.7	0.18	384,286	49.60	11.53
MUG-B16	157.0	150.5	2.0	3.085	0.091	16.8	0.17	384,286	49.60	11.53
MUG-B17	150.5	144.0	2.0	3.626	0.123	19.5	0.19	384,286	49.60	11.53
MUG-B18	144.0	136.5	2.0	3.209	0.140	16.3	0.16	384,286	49.60	11.53
MUG-B19	136.5	130.0	2.0	3.100	0.129	15.3	0.15	384,286	49.60	11.53
MUG-B20	130.0	123.5	2.0	2.762	0.095	13.7	0.14	384,286	49.60	11.53
MUG-B21	123.5	116.5	2.0	3.024	0.129	13.5	0.13	384,286	49.60	11.53
MUG-B22	116.5	109.5	2.0	3.004	0.119	12.3	0.12	384,286	49.60	11.53
MUG-B23	109.5	103.5	2.0	2.826	0.087	11.7	0.12	384,286	49.60	11.53
MUG-A01	122.5	117.5	2.0	3.287	0.100	14.2	0.14	382,823	49.32	11.59
MUG-A02	117.5	112.5	2.0	3.039	0.108	12.0	0.12	386,429	50.06	11.42
MUG-A03	112.5	107.5	2.0	2.883	0.129	10.1	0.10	380,714	49.41	11.57
MUG-A04	107.5	101.5	2.0	2.902	0.085	12.3	0.12	385,714	48.39	11.81

Table 3. *Cont.*

Sample Name	Top Position (cm)	Bottom Position (cm)	Thickness (cm)	^{36}Cl * (105 at/g)	^{36}Cl Uncertainty * (105 at/g)	Cl Total * (ppm)	Cl Total Uncertainty * (ppm)	Ca † (ppm)	O (%)	C (%)
MUG-A05	101.5	96.0	2.0	2.899	0.109	10.8	0.11	393,571	48.67	11.74
MUG-A06	96.0	91.0	2.0	2.838	0.118	12.7	0.13	391,429	49.60	11.53
MUG-A07	91.0	85.0	2.0	2.856	0.113	11.8	0.12	384,286	49.41	11.57
MUG-A08	85.0	79.0	2.0	2.726	0.083	10.1	0.10	385,714	49.60	11.53
MUG-A09	79.0	73.0	2.0	2.803	0.108	11.3	0.11	384,286	49.88	11.46
MUG-A10	73.0	66.5	2.0	2.448	0.105	11.4	0.11	382,143	50.71	11.27
MUG-A11	66.5	59.0	2.0	2.598	0.080	11.4	0.11	375,714	49.60	11.53
MUG-A12	59.0	51.5	2.0	2.665	0.098	11.5	0.12	384,286	49.78	11.49
MUG-A13	51.5	45.0	2.0	2.507	0.075	11.4	0.11	382,857	49.60	11.53
MUG-A14	45.0	38.5	2.0	2.468	0.118	12.0	0.12	384,286	49.69	11.51
MUG-A15	38.5	31.0	2.0	2.531	0.098	11.7	0.12	383,571	49.78	11.49
MUG-A16	31.0	24.5	2.0	2.409	0.069	11.2	0.11	382,857	50.06	11.42
MUG-A17	24.5	19.0	2.0	2.563	0.073	11.3	0.11	380,714	50.15	11.40
MUG-A18	19.0	13.0	2.0	2.626	0.102	11.1	0.11	380,000	50.25	11.38
MUG-A19	13.0	7.5	2.0	2.259	0.075	10.8	0.11	379,286	49.60	11.53
MUG-A20	7.5	4.5	2.0	2.225	0.068	12.7	0.13	384,286	50.34	11.36
MUG-A21	4.5	0.0	1.0	2.540	0.091	12.7	0.13	378,571	51.64	11.06

* Measured with accelerator mass spectrometry (AMS). † Measured with inductively coupled plasma mass spectrometry (ICP-MS).

Table 4. Average chemical composition of the bedrock and colluvium of the Manastır (this study) and Mugırtepe (modified after [24]) fault scarps used in earthquake modeling.

Fault	Cl, ppm	O, ppm	C, ppm	Na, ppm	Mg, ppm	Al, ppm	Si, ppm	P, ppm	K, ppm
Manastır	10.8	520,796	104,037	445	20,718	1398	4051	218	398
Mugırtepe	13.4	496,184	115,237	371	2593	344	491	196	166
	Ca, ppm	Ti, ppm	Mn, ppm	Fe, ppm	B, ppm	Sm, ppm	Gd, ppm	U, ppm	Th, ppm
Manastır	346,790	72	39	1022	3.4	0.24	0.7	1.16	0.18
Mugırtepe	384,123	30	39	210	1.5	0.05	0.025	0.565	0.05

Note: Cl is measured with accelerator mass spectrometry (AMS), the rest are measured with inductively coupled plasma mass spectrometry (ICP-MS). Average chemical composition is determined from representative samples.

We reanalyzed the Mugırtepe fault data reported by Akçar et al. [24] using the FSDT [37] by applying relatively more precise bottom and top positions of the samples rather than their heights along the sampling profile. Moreover, the calcium concentrations of the individual samples were used in the simulation. In this study, as we remodeled the Mugırtepe fault, which was formerly examined by Akçar et al. [24] using the Schlagenhauf et al. [22] code, it is useful to outline the main differences between the two modeling strategies. With respect to cosmic ray shielding by the fault scarp, while the Schlagenhauf code [22] applies scarp shielding only to neutron spallation, the FSDT code considers all cosmogenic particles producing ^{36}Cl; that is neutron spallation, fast muons, and thermal and epithermal neutrons (cf. [26,37]). In addition, in the Schlagenhauf code, one exponential simplification of muon attenuation is considered, whereas the FSDT approach uses the full model by Heisinger et al. [79,80]. Moreover, considering the exact position of bottom and top of the samples along the fault surface in FSDT is required to obtain more accurate results in terms of distributions of particles at nodes of three-dimensional mesh. This provides coverage of all possible positions of the sample strip to calculate the theoretical ^{36}Cl, which might have been produced. Dimensions of mesh are considered as the depth of sample perpendicular to scarp surface, the position of the samples along the fault surface and the relative position of footwall and colluvium wedge. These differences affect the model outputs with differences of a few percentage points. The FSDT code applies a broad-ranging search for the optimal solution using the Monte-Carlo method. In addition, despite both codes apply forward modeling, the FSDT method uses a two-step modeling

process whereby a database is created during the first step, which has the advantage of reducing the simulation running time.

4. Results

4.1. Cosmogenic ^{36}Cl Concentration Analysis

The fault scarp parameters used for the database and default rates of ^{36}Cl production are presented in Table 1. The samples positions, thicknesses, cosmogenic ^{36}Cl and natural Cl values and uncertainties, calcium, oxygen, and carbon contents are provided in Tables 2 and 3 for the Manastır and Mugırtepe faults, respectively. The average compositions of major and trace elements of the bedrock and colluvium are listed in Table 4.

4.2. Time-Slip Histories of the Manastır and Mugırtepe Fault Scarps

Our best-fit model for the Manastır and Mugırtepe faults yields two and one earthquake(s), respectively (Table 5). The best-fit solution resulting from the simulation of the Manastır dataset indicates seismic events at 3.5 ± 0.9 ka and 2.0 ± 0.5 ka, with the beginning of accumulation at 8.8 ka (Figure 7). The modeled slips for these events are 3.3 ± 0.5 m and 3.6 ± 0.5 m, respectively. The Akaike information criterion (AICc) of this simulation was 444.46, the weighted root-mean-square (RMSw) was 2.12, and the chi-square (χ2) value was 4.91 (Table 5). The incremental slip rate of 2.2 mm yr^{-1} is calculated for the time interval between the first and second modeled earthquakes, and 1.8 mm yr^{-1} between the second earthquake and the present. The average slip rate of 1.9 mm yr^{-1} is estimated based on a 6.7-m cumulative throw since the oldest modeled earthquake (Figure 8).

Table 5. Best fit results for the modeling of the Manastır and Mugırtepe fault scarps dataset.

Fault	Beginning of Accumulation (ka)	Age (ka)	Slip (cm)	Throw/Maximum Vertical Displacement (cm)	IncrementalSlip Rate (mm yr^{-1})	Average Slip Rate (mm yr^{-1})	X^2	AICc	RMSw
Manastır	8.8	2.0 ± 0.5 3.5 ± 0.9	3.6 ± 0.5 3.3 ± 0.5	3.5 ± 0.5 3.2 ± 0.5	2.2 1.8	1.9	4.91	444.46	2.12
Mugırtepe	27.0	6.5 ± 1.6	2.7 ± 0.4	2.1 ± 0.3	0.3	0.3	1.88	178.31	1.31

Note: Slip rates are calculated using the maximum vertical displacement (e.g., throw).

The re-analysis of the Mugırtepe fault data from Akçar et al. [24] showed a single seismic event at 6.5 ± 1.6 ka, with the beginning of exposure at 27 ka and a vertical slip of 2.7 ± 0.4 m (Figure 9). For this single-earthquake scenario, the best-fit (AICc) analysis yielded a value of 178.31, RMSw a value of 1.31, and χ^2 a value of 1.88 (Table 5). A slip rate of 0.3 mm yr^{-1} was calculated based on maximum vertical displacement divided by the age of the modeled seismic event (Figure 10). Because the upper parts of both the Manastır and Mugırtepe faults were not suitable for sampling, it should be noted that the number of reconstructed seismic events is minimum.

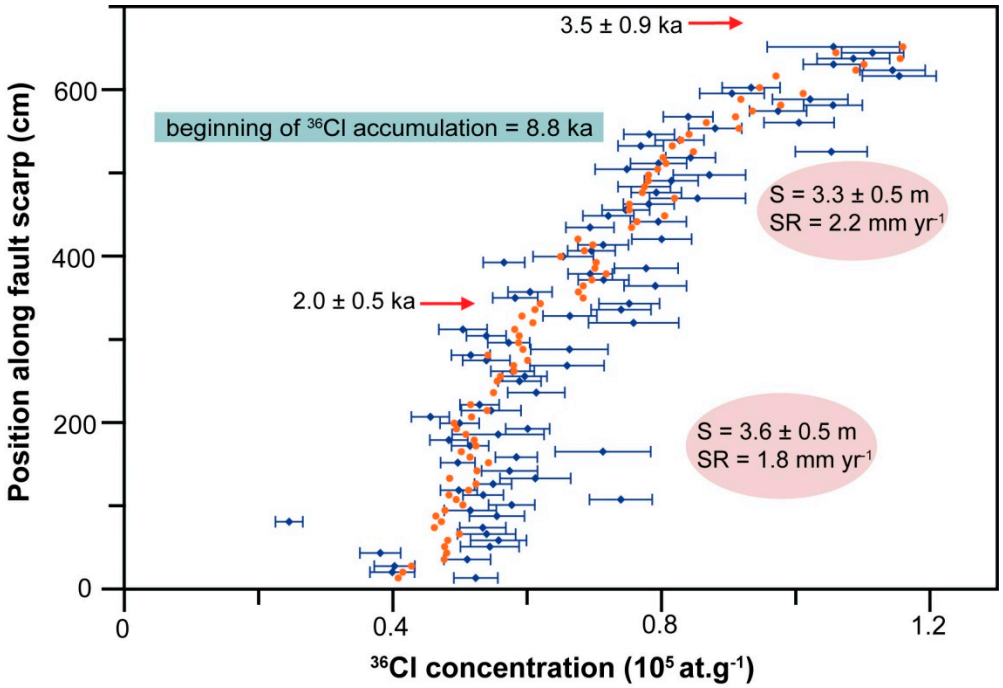

Figure 7. Best fit (filled circles) of the data for the samples from the Manastır fault scarp with a two seismic event model and beginning of ^{36}Cl accumulation ca. 8.8 ka. Dots with 2σ uncertainties are measured ^{36}Cl concentrations. The arrows mark the colluvium positions before the modeled seismic event. S and SR define the amount of slip and incremental slip rate, respectively.

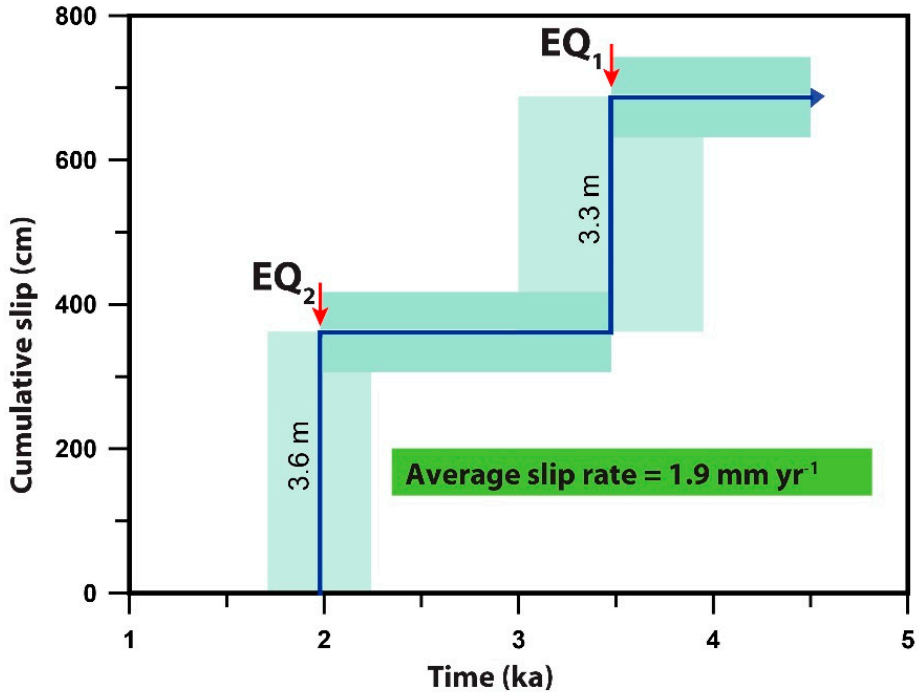

Figure 8. Cumulative slip versus time. Green bands indicate the uncertainties of seismic events ages and colluvium level obtained from modeling of Manastır fault; the average slip rate is 1.9 mm yr^{-1}.

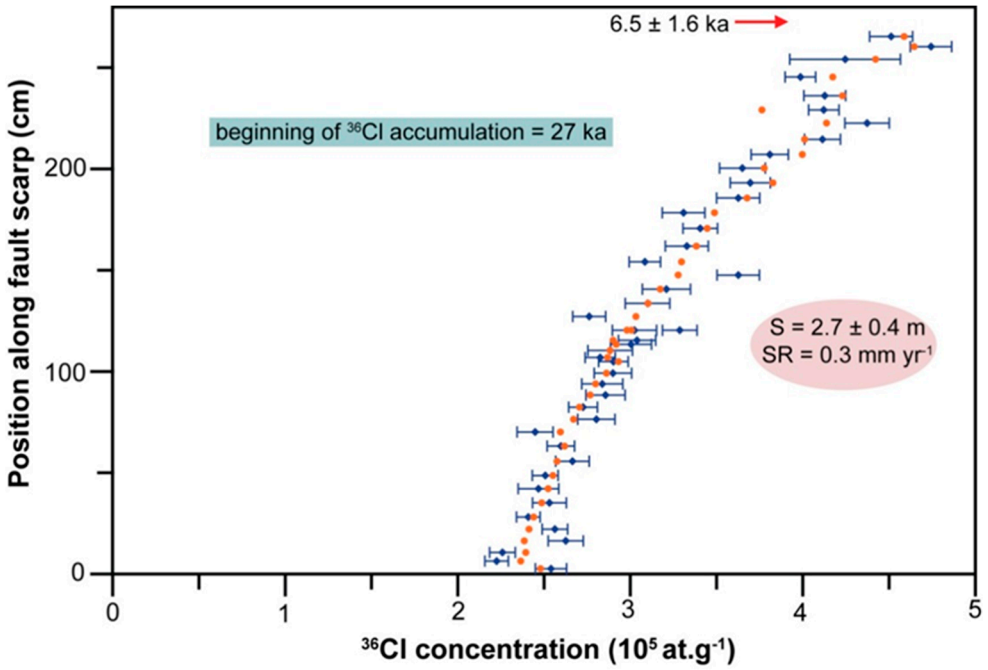

Figure 9. Best fit (filled circles) of the data for the samples from the Mugırtepe fault scarp with a single seismic event model and beginning of ^{36}Cl accumulation ca. 27 ka. Dots with 2σ uncertainties are measured ^{36}Cl concentrations. The arrow marks the colluvium positions before the modeled seismic event. S and SR define the amount of slip and incremental slip rate, respectively.

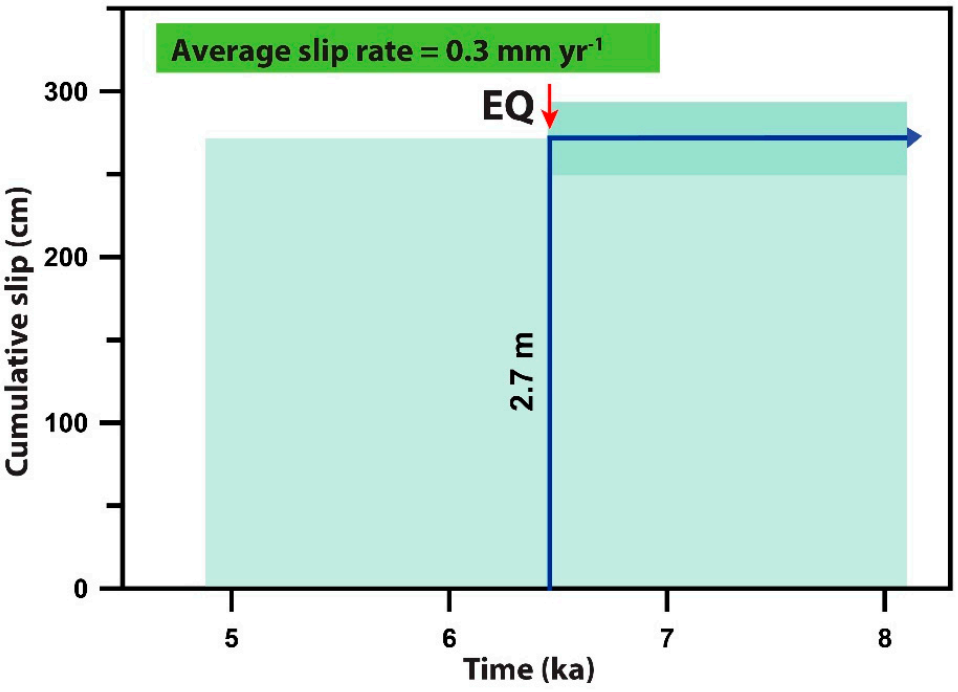

Figure 10. Cumulative slip versus time. Green bands show the uncertainties of seismic events ages and colluvium level obtained from modeling of Mugırtepe fault; the average slip rate is 0.3 mm yr^{-1}.

5. Discussion

5.1. Plausibility of Earthquake Modeling

The modeling of seismic events associated with the Mugırtepe and Manastır faults indicates that both faults slipped during the Holocene. As mentioned above, these faults are

elements of the MFZ, therefore they must have moved in response to slip on this fault zone at 6.5 ± 1.6, 3.5 ± 0.9 and 2.0 ± 0.5 ka. The modeled seismic event at 6.5 ± 1.6 ka is close to that of the youngest earthquake modeled by Akçar et al. [24]. Based on the assumption that the Manastır fault is the principal slip surface of the fault zone, we suggest that this event (and probably the older one(s)) was recorded in the upper 5 m of the Manastır fault scarp. We support this argument by comparing measured the cosmogenic ^{36}Cl concentrations and timing of modeled seismic events of Manastır and Mugırtepe faults. The chemical compositions of Mugırtepe and Manastır samples, especially ^{40}Ca concentrations as the main target of cosmogenic ^{36}Cl production, are very similar (Tables 2 and 3) and the longer is the fault surface exposed, the more concentration of cosmogenic ^{36}Cl is expected. We assume that the accumulation pattern of the measured cosmogenic ^{36}Cl concentrations on the Manastır fault (Figure 7) is similar to the accumulation pattern on the Mugırtepe fault (Figure 9). Therefore, we expect that the cosmogenic ^{36}Cl concentrations on the higher unsampled surface of the Manastır fault (>6.5 m), if it was possible to measure, should increase upscarp surface and be relatively close to those on the Mugırtepe fault scarp. However, no chronology can be attributed to this unsampled section with a high degree of certainty, owing poor surface preservation for sampling.

Here, we discuss the fault parameters that arise from our modeling by applying empirical relationships (Table 6) that link the modeled earthquake magnitudes to the surface rupture lengths and displacements [50,81,82]. Theoretically, the instantaneous rupture of the entire 35-km-long MFZ would have required an earthquake with a magnitude of approximately 6.9 and an average slip amount of 1–1.7 m regardless of modeling [50,81,82] (Table 6). By considering Equation (6) in Table 6, the maximum slip of 3.1 m for MFZ was calculated, which fits to the lower bound of modeled slip, though is the most appropriate approach in this case. Therefore, our modeled slips of over 3 m can probably be explained by at least two large-magnitude earthquakes (>6) occurring over a short time span within the uncertainty of modeled ages. However, such concurrent earthquakes cannot be differentiated by the FSDT or any other code or recognized as separate events (cf. [22,37]). We assert the occurrence of clustered earthquake in a close time, because in addition to theoretical calculations above, basically the amount of displacement close to tips of the normal faults is smaller than that around the fault's center (e.g., [83–85]). We propose that the earthquakes that occurred in the MFZ triggered the synchronous displacement of all or some of the main segments of the fault zone, including the Manastır master fault, which in turn resulted in the exposure of secondary fault scarps such as the Mugırtepe.

Table 6. Regression of SRL (surface rupture length), magnitude (Ms/M) and vertical displacement (MVD/MD) values calculated for the Manastır and Mugırtepe faults and the Manisa Fault Zone.

SRL/FL		**35 km**
Sin (θ) = Maximum Vertical Displacement/Slip		**Manisa Fault Zone (avg. θ = 60°)**
[50]	Ms = 0.9 × Log (SRL) + 5.48	6.9
	Log (MVD) = 1.14 × Ms − 7.82	MVD = 1.0; Slip ~ 1.3
[81]	M = 4.86 + 1.32 × log (SRL)	6.9
	Log (MD) = −5.90 + 0.89 × M	MD (Slip) = 1.7
[82]	Mw = 6.12 + 0.47 × log (SRL)	6.9
	Maximum Slip = 0.09 × SRL Average slip = 0.03 × SRL	Maximum slip = 3.1 Average slip = 1.0

Note: The unit of slip, MVD and MD is in meters. MVD (maximum vertical displacement) is converted to slip or MD (maximum displacement) by applying fault surface dip (sin (θ) = Maximum vertical displacement/slip).

The time span of the modeled seismic events covers a part of the activity of the MFZ during the Holocene, extending the seismic archives significantly beyond the historical records. Indeed, the youngest modeled seismic event at 2.0 ± 0.5 ka temporarily coincides with the most devastating historical earthquake in this region. Many ancient cities within

the Manisa Basin and its environs were damaged or completely destroyed in 17 AD by an earthquake with an intensity of IX [3] and a reconstructed Mw of 7.4 (e.g., [57]). Shortly after, in 44 AD, another event with an intensity of VIII damaged the ancient cities of Magnesia and Ephesus [66]. Considering the rough magnitude value of an earthquake possibly sourced by the 35-km-long MFZ (Mw 6.9) and slip (1–3.1 m), we argue that the 17 AD earthquake is a reliable candidate for the event at 2.0 ± 0.5 ka. The earthquake of 44 AD is mainly attributed to rupture the southern faults close to Izmir and Kemalpaşa (Figure 2); Thus, the 3.6 ± 0.5 m rupture of the Manastır fault scarp is triggered by earthquake of the 17 AD event and probably a smaller unrecorded earthquake.

Our modeling did not yield any seismic event younger than 2.0 ± 0.5 ka. At least three additional historical destructive earthquakes, which caused damages in the region, have been reported: the 926 AD, 1595/1664 AD, and 1845 AD events (Figure 2). The epicenter location of the earthquake of 926 AD similar to that of 44 AD appears to be associated with the faults in the south. Moreover, the reconstructed epicenters of the 1595/1664 AD events are located on the eastern part of the southern main boundary of the Gediz Graben and the Izmir fault, respectively (Figure 2) [3,48,58]. In addition, the 1845 AD earthquake, with an epicenter to the east of Manisa is not a definitive earthquake and considered as extreme exaggeration of June 5, 1845 AD Izmir earthquake. The evidence of this event is missing in the Church Missonary Society archives for 1845–46 AD damages of the Izmir–Manisa region [1]. Ambraseys [1] states that this earthquake is only reported by Perrey [86], which claims several weeks before July 23, Manisa was completely destroyed by an earthquake, and this was accordingly reported in modern earthquake catalogues. The abovementioned earthquakes must have initiated significant rupturing of nearby faults but, most likely, negligible or zero rupturing of more distal faults, such as MFZ. However, these events left evidence of liquefaction and lateral spreading in the colluvium in front of the Mugırtepe fault; but their impact in terms of surface rupture or dip-slip displacement of the fault is unclear owing to a lack of field data [59]. These findings could be directly related to availability of organic material, however further discussion regarding the possibilities is beyond the scope of this study.

5.2. Evolution of the Western Manisa Fault Zone

There is a dearth of information about the timing of the initiation of surface rupture of the Manastır fault, which is the main and longest fault in the western MFZ. According to radiocarbon dating of charcoal samples in palaeosol and bulk sediment samples from the Emlakdere Formation, the progressive accumulation and tilting of the Emlakdere Formation in front of the Manastır fault in the hanging-wall began ca. 19 cal kyr BP [59], which can be considered as the lower bound for the initial surface rupture of the Manastır fault (Figure 11). Deposition and progressive tilting of hanging-wall deposits are indicated by diverse dip of bedding planes of the Emlakdere Formation. This syn-sedimentary faulting continued until ca. 9 cal kyr BP based on the ^{14}C age of a palaeosol sample collected from the uppermost part of the Emlakdere Formation within the hanging-wall of F1, where the dip-slip offset of Emlakdere block is a minimum of 12 m (Figure 11) [59]. The time span of sedimentation (from ca. 19 to 9 ka) in this area correlates with the timing of Last Glacial Maximum (LGM) and Termination-I in the northern hemisphere [87–89], when the rate of sedimentation is assumed to be rapid. This implies that the rupture of the secondary faults in the Manisa basin (F1 to F4 including the Mugirtepe Fault) should have initiated after ca. 9 ka. Based on these lines of evidence, we argue that activity of F1, similarly to all the other secondary faults, are younger than surface rupture of the Manastır fault.

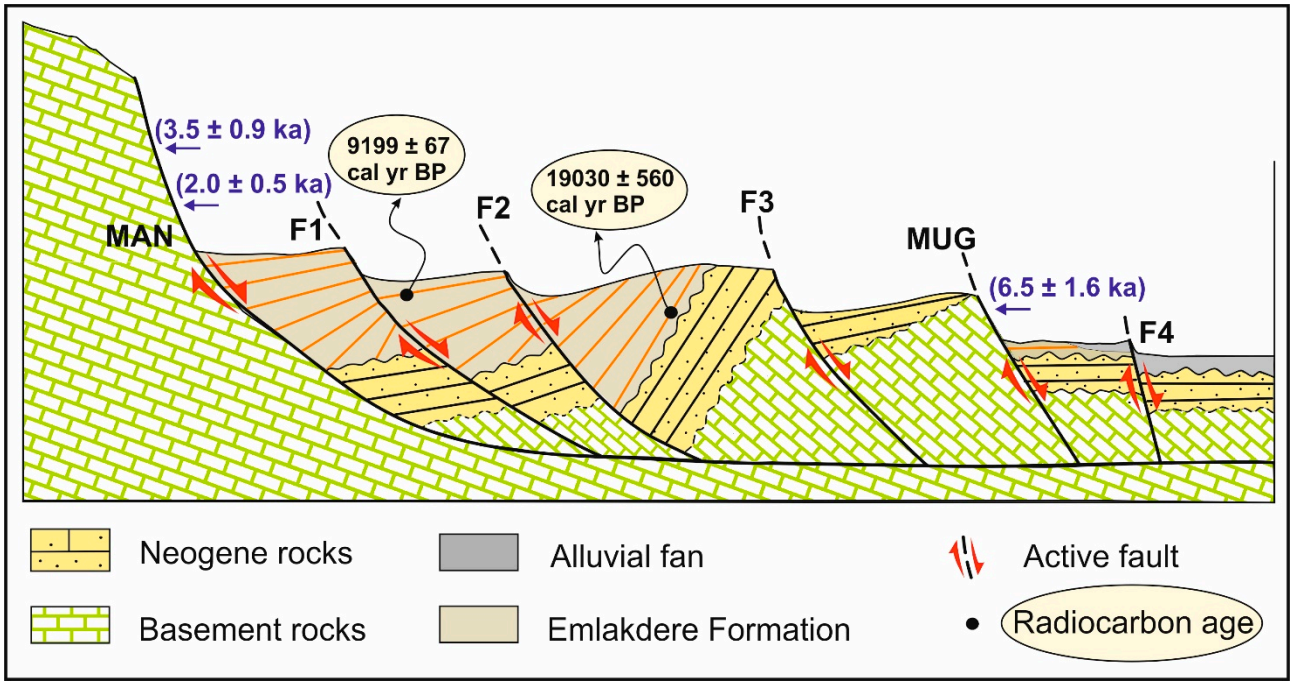

Figure 11. Simplified schematic sketch showing western Manisa Fault Zone and its synthetic faults displacing formations of various ages (Early-late Holocene). Note that in the cartoons the exact horizontal and vertical scales, vertical displacement values as well as thickness of sedimentary layers are disregarded. The approximate lateral distance between MAN and F4 is 400 m. MAN fault depth is 5–10 km at about 10 km northeast of Manisa. MAN: Manastır fault, MUG: Mugırtepe fault. Radiocarbon ages are taken from study of Özkaymak et al. [59], as ca. 19 and 9 cal kyr BP, representing the lowermost and uppermost paleosols within the Emlakdere formation, respectively.

Back-tilting of bedding planes in the hangingwall of the faults, in general decreases towards the basin. Accordingly, we plead that the closest faults to the Manastır fault experienced most likely more earthquakes and higher subsequent slip than those close to the basin. Among those, hangingwall of F2 accommodates the highest backtilting, while the MUG and F4 are characterized by sub-horizontal bedding planes in their hangingwalls. This reveals that most likely not all secondary faults are affected by seismic event simultaneously. Although F4 was not dated in this study, there is field evidence that a Late Holocene alluvial fan is displaced by F4 (Figures 3 and 4). Though, we interpret that F4 was broken by a younger activity than that of responsible for Mugırtepe fault rupture, presumably synchronized with Manastır fault activity either at ca. 3.5 or 2 ka. The deformation of the alluvial fan by F4, which overlies the Mugırtepe fault, assures that F4 ruptured later than the Mugırtepe fault. This sequence of events might be a hint for the basinward migration of the faulting. However, the evolution of the faulting in the Manisa Fault Zone remains obscure and needs to be explored by additional dating studies.

Nevertheless, we propose that the Manastır and Mugırtepe faults could underwent number of earthquakes between ca. 9 cal kyr BP and 6.5 ± 1.6 ka. These should have resulted in associated slips, which are obscured today in the poorly preserved upper 5 m and 1.3 m of these faults. The seismic event at 6.5 ± 1.6 ka displaced the Mugırtepe secondary fault by 2.7 ± 0.4 m, as revealed by our modeling (Figure 11). This event might have occurred as two clustered earthquakes in the Manastır master fault that caused the simultaneous displacement of the Mugırtepe fault, if this is true, these ruptures should presumably be recorded in the current upper 5 m of the Manastır fault. At 3.5 ± 0.9 ka, the Manastır fault moved by 3.3 ± 0.5 m as a result of several subsequent earthquakes, which appear not to cause any movement of the Mugırtepe fault. The Manastır fault experienced another seismic event at 2.0 ± 0.5 ka with a significant displacement of 3.6 ± 0.5 m (Figure 11), which we attribute to the destructive earthquakes of 17 AD and a probable smaller event missing in historical records (Figure 11).

5.3. Timing of Seismically Active Periods in Western Anatolia

Using fault scarp dating, we reconstructed the oldest discovered seismic event in MFZ at 6.5 ± 0.5 ka followed by the subsequent event at 3.5 ± 0.9 ka. The subsequent modeled earthquake at 2.0 ± 0.5 ka temporally coincides with the 17 destructive earthquakes recorded in the historic records.

We showed that MFZ was active during Holocene similar to other faults in the region (cf. [33,34]). The 2.0 ± 0.5 ka earthquake is highly concordant with the timing of the youngest earthquakes discovered using fault scarp dating on the Yavansu, Priene-Sazlı, and Ören faults (Figure 1). In addition to the Rahmiye fault, all of these faults are considered to have been activated in a close time by the modeled Manastır fault earthquake at 3.5 ± 0.9 ka. Similarly, the timing of the reconstructed earthquake at 6.5 ± 1.6 ka for the Mugırtepe fault is compatible with the age of the reconstructed earthquakes of the Priene-Sazlı and Ören faults. Overall, our fault scarp dating shows that regional seismic activity in Western Anatolia has a rhythmic pattern and is broadly characterized by clusters of surface rupturing earthquakes with phases of high seismic activities with a recurrence interval of ca. 2000 yr.

6. Conclusions

Fault scarp dating in the western MFZ has been observed to be a means of exploring major earthquake events. We documented the occurrence of two and one seismic events, respectively, for the Manastır and Mugırtepe faults as a component of the MFZ during the Holocene. Each of these events is considered to result from clustered earthquakes with the modeled displacements representing the cumulative slip due to these events. The youngest of these events coincides with earthquakes documented in the historic record at 17. The reconstructed earthquakes associated with the Mugırtepe fault are interpreted to have occurred as a consequence of activity on the Manastır fault. While both the Manastır and Mugırtepe faults are tectonic, the former is considered to be seismogenic and the latter non-seismogenic. Our results together with the geological and paleoseismological investigations [59] demonstrate that in the western MFZ, the hangingwall of the master Manastır fault experienced syn-depositional rotation during the Late Pleistocene-early Holocene. Thereafter, secondary faults developed during the Early–late Holocene as a consequence of repeated earthquakes. Our results can unfortunately not solve the growth of the secondary faults. Whether they display a migration pattern or irregular rupture pattern remains to be explored. Our findings are consistent with previous fault scarp dating results from western Turkey [33–35]. This demonstrates the significant potential of this method for deriving the critical parameters required for precise evaluations of seismic risk.

Supplementary Materials: The following are available online at https://www.mdpi.com/article/10.3390/geosciences11110451/s1.

Author Contributions: Conceptualization, N.M., Ç.Ö., D.T., V.A., S.I.-O., H.S., C.S. and N.A.; methodology, D.T. and N.A.; software, D.T.; validation, N.M. and N.A.; formal analysis, N.M.; investigation, N.M., D.T. and N.A.; resources, Ç.Ö., S.I.-O., V.A., H.S., C.S. and N.A.; data curation, N.A.; writing—original draft preparation, N.M. and D.T.; writing—review and editing, N.M. and N.A.; visualization, N.M. and Ç.Ö.; supervision, H.S. and N.A.; project administration, N.A.; funding acquisition, H.S. and N.A.; All authors have read and agreed to the published version of the manuscript.

Funding: This research was funded by Dokuz Eylul University, Turkey [Research Project No. 2007.KB.FEN.047 and 2008.KB.FEN.008]; the Surface Exposure Dating Laboratory, University of Bern, Switzerland; the Bern University Research Foundation and the Swiss National Science Foundation, Switzerland [Project No. 200021-147065].

Data Availability Statement: Data required for simulation including FSDT code, excel files, and databases for both faults are provided as Supplementary Material.

Acknowledgments: We would like to specially thank the Laboratory of Ion Beam Physics operated by the Swiss Federal Institute of Technology, Zurich, Switzerland. We are grateful to Bora Uzel and Onur Sarıoğlu for their help during field studies. We especially acknowledge the constructive comments and feedback given by three anonymous reviewers.

Conflicts of Interest: The authors declare no conflict of interest.

References

1. Ambraseys, N. *Earthquakes in the Mediterranean and Middle East: A Multidisciplinary Study of Seismicity up to 1900*; Cambridge University Press: Cambridge, UK, 2009; p. 947.
2. Shebalin, N.V.; Karnik, V.; Hadzievski, D. *Catalogue of Earthquakes of the Balkan Region. I, UNDP-UNESCO Survey of the Seismicity of the Balkan Region*; UNDP: Skopje, Yugoslavia, 1974; p. 600.
3. Soysal, H.; Sipahioğlu, S.; Kolçak, D.; Altınok, Y. *Historical Earthquake Catalogue of Turkey and Surrounding Area (2100 B.C.–1900 A.D.)*; Technical Report, TÜBİTAK, No. TBAG-341; The Scientific and Technological Research Council of Turkey: Ankara, Turkey, 1981.
4. Papadopoulos, G.A. A Seismic History of Crete: Earthquakes and Tsunamis 2000 B.C.–2011 A.D. *Ocelotos Publ.* **2011**, *65*, 415.
5. England, P.; Jackson, J.A. Uncharted seismic risk. *Nat. Geosci.* **2011**, *4*, 348–349. [CrossRef]
6. Stein, S.; Friedrich, A.M. How much can we clear the crystal ball? *Astron. Geophys.* **2014**, *55*, 2.11–2.17. [CrossRef]
7. Konstantinou, K.I.; Mouslopoulou, V.; Saltogianni, V. Seismicity and Active Faulting around the Metropolitan Area of Athens, Greece. *Bull. Seismol. Soc. Am.* **2020**, *110*, 1924–1941. [CrossRef]
8. Morley, C.K. Patterns of displacement along large normal faults; implications for basin evolution and fault propagation, based on examples from East Africa. *Am. Assoc. Pet. Geol. Bull.* **1999**, *83*, 613–634.
9. Biasi, G.P.; Weldon, R.J.; Fumal, T.E.; Seitz, G.G. Paleoseismic event dating and conditional probability of large earthquakes on the southern San Andreas fault, California. *Bull. Seismol. Soc. Am.* **2002**, *92*, 2761–2781. [CrossRef]
10. Nicol, A.; Walsh, J.; Berryman, K.; Villamor, P. Interdependence of fault displacement rates and paleoearthquakes in an active rift. *Geology* **2006**, *34*, 865–868. [CrossRef]
11. Nicol, A.; Walsh, J.J.; Villamor, P.; Seebeck, H.; Berryman, K.R. Normal fault interactions, paleoearthquakes and growth in an active rift. *J. Struct. Geol.* **2010**, *32*, 1101–1113. [CrossRef]
12. Berryman, K.R.; Villamor, P.; Nairn, I.A.; Van Dissen, R.J.; Begg, J.G.; Lee, J.M. Late Pleistocene surface rupture history of the Paeroa Fault, Taupo Rift, New Zealand. *N. Z. J. Geol. Geophys.* **2008**, *51*, 135–158. [CrossRef]
13. Friedrich, A.M.; Lee, J.; Wernicke, B.P.; Sieh, K. Geologic context of geodetic data across a Basin and Range normal fault, Crescent Valley, Nevada. *Tectonics* **2004**, *23*, TC2015. [CrossRef]
14. Mouslopoulou, V.; Nicol, A.; Walsh, J.J.; Begg, J.G.; Townsend, D.B.; Hristopulos, D.T. Fault-slip accumulation in an active rift over thousands to millions of years and the importance of paleoearthquake sampling. *J. Struct. Geol.* **2012**, *36*, 71–80. [CrossRef]
15. Zreda, M.; Noller, J.S. Ages of prehistoric earthquakes revealed by cosmogenic chlorine-36 in a bedrock fault scarp at Hebgen Lake. *Science* **1998**, *282*, 1097–1099. [CrossRef]
16. Mitchell, S.G.; Matmon, A.; Bierman, P.R.; Enzel, Y.; Caffee, M.; Rizzo, D. Displacement history of a limtesone normal fault scarp, northern Israel, from cosmogenic ^{36}Cl. *J. Geophys. Res.* **2001**, *106*, 4247–4264. [CrossRef]
17. Benedetti, L.; Finkel, R.; King, G.; Armijo, R.; Papanastassiou, D.; Ryerson, F.J.; Flerit, F.; Farber, D.; Stavrakakis, G. Motion on the Kaparelli fault (Greece) prior to the 1981 earthquake sequence determined from Cl-36 cosmogenic dating. *Terra Nova* **2003**, *15*, 118–124. [CrossRef]
18. Benedetti, L.; Finkel, R.; Papanastassiou, D.; King, G.; Armijo, R.; Ryerson, F.; Farber, D.; Flerit, F. Post-glacial slip history of the Sparta fault (Greece) determined by Cl-36 cosmogenic dating: Evidence for non-periodic earthquakes. *Geophys. Res. Lett.* **2002**, *29*, 87-1–87-4. [CrossRef]
19. Benedetti, L.; Manighetti, I.; Gaudemer, Y.; Finkel, R.; Malavieille, Y.; Pou, K.; Arnold, M.; Aumaître, G.; Bourlès, D.; Keddadouche, K. Earthquake synchrony and clustering on Fucino faults (Central Italy) as revealed from in situ ^{36}Cl exposure dating. *J. Geophys. Res. Solid Earth* **2013**, *118*, 4948–4974. [CrossRef]
20. Palumbo, L.; Benedetti, L.; Bourles, D.; Cinque, A.; Finkel, R. Slip history of the Magnola fault (Apennines, Central Italy) from ^{36}Cl surface exposure dating: Evidence for strong earthquake over the Holocene. *Earth Planet. Sci. Lett.* **2004**, *225*, 163–176. [CrossRef]
21. Carcaillet, J.; Manighetti, I.; Chauvel, C.; Schlagenhauf, A.; Nicole, J.M. Identifying past earthquakes on an active normal fault (Magnola, Italy) from the chemical analysis of its exhumed carbonate fault plane. *Earth Planet. Sci. Lett.* **2008**, *271*, 145–158. [CrossRef]
22. Schlagenhauf, A.; Gaudemer, Y.; Benedetti, L.; Manighetti, I.; Palumbo, L.; Schimmelpfennig, I.; Finkel, R.; Pou, K. Using in situ Chlorine-36 cosmonuclide to recover past earthquake histories on limestone normal fault scarps: A reappraisal of methodology and interpretations. *Geophys. J. Int.* **2010**, *182*, 36–72. [CrossRef]
23. Schlagenhauf, A.; Manighetti, I.; Benedetti, L.; Gaudemer, Y.; Finkel, R.; Malavieille, J.; Pou, K. Earthquake supercycles in Central Italy, inferred from ^{36}Cl exposure dating. *Earth Planet. Sci. Lett.* **2011**, *307*, 487–500. [CrossRef]

24. Akçar, N.; Tikhomirov, D.; Özkaymak, Ç.; Alfimov, V.; Ivy-Ochs, S.; Sözbilir, H.; Uzel, B.; Schlüchter, C. ^{36}Cl Exposure dating of paleoearthquakes in the Eastern Mediterranean: First results from Western Anatolian Extensional Province, Manisa Fault Zone, Turkey. *Geol. Soc. Am. Bull.* **2012**, *124*, 1724–1735. [CrossRef]
25. Mouslopoulou, V.; Moraetis, D.; Benedetti, L.; Guillou, V.; Bellier, O.; Hristopulos, D. Normal faulting in the forearc of the Hellenic subduction margin: Paleoearthquake history and kinematics of the Spili Fault, Crete, Greece. *J. Struct. Geol.* **2014**, *66*, 298–308. [CrossRef]
26. Tikhomirov, D.; Akçar, N.; Ivy-Ochs, S.; Alfimov, V.; Schlüchter, C. Calculation of shielding factors for production of cosmogenic nuclides in fault scarps. *Quat. Geochronol.* **2014**, *19*, 181–193. [CrossRef]
27. Tikhomirov, D. An Advanced Model for Fault Scarp Dating and Paleoearthquake Reconstruction, with a Case Study of the Gediz Graben Formation (Turkey). Ph.D. Thesis, University of Bern, Bern, Switzerland, 2014; p. 113.
28. Kong, P.; Fink, D.; Chunguang, N.; Xiao, W. Dip-slip rate determined by cosmogenic surface dating on a Holocene scarp of the Daju fault, Yunnan, China. *Tectonophysics* **2010**, *493*, 106–112. [CrossRef]
29. Tesson, J.; Pace, B.; Benedetti, L.; Visini, F.; Delli Rocioli, M.; Arnold, M.; Aumaître, G.; Bourlès, D.L.; Keddadouche, K. Seismic slip history of the Pizzalto fault (central Apennines, Italy) using in situ-produced ^{36}Cl cosmic ray exposure dating and rare earth element concentrations. *J. Geophys. Res. Solid Earth* **2016**, *121*, 1983–2003. [CrossRef]
30. Cowie, P.A.; Phillips, R.J.; Roberts, G.P.; McCaffrey, K.; Zijerveld, L.J.J.; Gregory, L.C.; Faure Walker, J.; Wedmore, L.N.J.; Dunai, T.J.; Binnie, S.A.; et al. Orogen-scale uplift in the central Italian Apennines drives episodic behaviour of earthquake faults. *Sci. Rep.* **2017**, *7*, 44858. [CrossRef]
31. Beck, J.; Wolfers, S.; Roberts, J.P. Bayesian earthquake dating and seismic hazard assessment using chlorine-36 measurements (BED v1). *Geosci. Model Dev.* **2018**, *11*, 4383–4397. [CrossRef]
32. Mechernich, S.; Schneiderwind, S.; Mason, J.; Papanikolaou, I.D.; Deligiannakis, G.; Pallikarakis, A.; Reicherter, K. The seismic history of the Pisia fault (eastern Corinth rift, Greece) from fault plane weathering features and cosmogenic ^{36}Cl dating. *J. Geophys. Res. Solid Earth* **2018**, *123*, 4266–4284. [CrossRef]
33. Mozafari, N.; Sümer, Ö.; Tikhomirov, D.; Ivy-Ochs, S.; Alfimov, V.; Vockenhuber, C.; İnci, U.; Sözbilir, H.; Akçar, N. Holocene seismic activity of the Priene-Sazlı Fault revealed by cosmogenic ^{36}Cl, western Anatolia, Turkey. *Turk. J. Earth Sci.* **2019**, *28*, 410–437. [CrossRef]
34. Mozafari, N.; Tikhomirov, D.; Sümer, Ö.; Özkaymak, Ç.; Uzel, B.; Yeşilyurt, S.; Ivy-Ochs, S.; Vockenhuber, C.; Sözbilir, H.; Akçar, N. Dating of active normal fault scarps in the Büyük Menderes Graben (western Anatolia) and its implications for seismic history. *Quat. Sci. Rev.* **2019**, *220*, 111–123. [CrossRef]
35. Mozafari, N.; Özkaymak, Ç.; Sümer, Ö.; Tikhomirov, D.; Uzel, B.; Yeşilyurt, S.; Ivy-Ochs, S.; Vockenhuber, C.; Sözbilir, H.; Akçar, N. Seismic history of western Anatolia during the last 16 kyr determined by cosmogenic ^{36}Cl dating. *Swiss J. Geosci.* **2021**. in revision.
36. Tesson, J.; Benedetti, L. Seismic history from in situ ^{36}Cl cosmogenic nuclide data on limestone fault scarps using Bayesian reversible jump Markov chain Monte Carlo. *Quat. Geochronol.* **2019**, *52*, 1–20. [CrossRef]
37. Tikhomirov, D.; Mozafari, N.; Ivy-Ochs, S.; Alfimov, V.; Vockenhuber, C.; Akçar, N. Fault Scarp Dating Tool—A MATLAB code for fault scarp dating with in-situ chlorine-36 along with datasets of Yavansu and Kalafat faults. *Data Brief* **2019**, *26*, 104476. [CrossRef]
38. Goodall, H.J.; Gregory, L.C.; Wedmore, L.N.J.; McCaffrey, K.J.W.; Amey, R.M.J.; Roberts, G.P.; Shanks, R.P.; Phillips, R.J.; Hooper, A. Determining histories of slip on normal faults with bedrock scarps using cosmogenic nuclide exposure data. *Tectonics* **2021**, *40*, e2020TC006457. [CrossRef]
39. Crone, A.J.; Machette, M.N.; Bonilla, M.G.; Lienkaemper, J.J.; Pierce, K.L.; Scott, W.E.; Bucknam, R.C. Surface Faulting Accompanying the Borah Peak Earthquake and Segmentation of the Lost River Fault, Central Idaho. *Bull. Seismol. Soc. Am.* **1987**, *77*, 739–770.
40. Stewart, I.S.; Hancock, P.L. Normal fault zone evolution and fault scarp degradation in the Aegean region. *Basin Res.* **1988**, *1*, 139–153. [CrossRef]
41. Hancock, P.L.; Barka, A.A. Kinematic indicators on active normal faults in western Turkey. *J. Struct. Geol.* **1987**, *9*, 573–584. [CrossRef]
42. Sümer, Ö.; Inci, U.; Sözbilir, H. Tectonic evolution of the Söke Basin: Extension-dominated transtensional basin formation in western part of the Büyük Menderes Graben, Western Anatolia, Turkey. *J. Geodyn.* **2013**, *65*, 148–175. [CrossRef]
43. Sözbilir, H.; Sarı, B.; Uzel, B.; Sümer, Ö.; Akkiraz, S. Tectonic implications of transtensional supradetachment basin development in an extension-parallel transfer zone: The Kocaçay Basin, western Anatolia, Turkey. *Basin Res.* **2011**, *23*, 423–448. [CrossRef]
44. Özkaymak, Ç.; Sözbilir, H. Stratigraphic and structural evidence for fault reactivation: The active Manisa fault zone, western Anatolia. *Turk. J. Earth Sci.* **2008**, *17*, 615–635.
45. Uzel, B.; Sözbilir, H.; Özkaymak, Ç.; Kaymakçı, N.; Langeris, C.G. Structural evidence for strike-slip deformation in the İzmir-Balıkesir Transfer Zone and consequences for late Cenozoic evolution of western Anatolia (Turkey). *J. Geodyn.* **2013**, *65*, 94–116. [CrossRef]
46. Özkaymak, Ç.; Sözbilir, H.; Uzel, B. Neogene–Quaternary evolution of the Manisa Basin: Evidence for variation in the stress pattern of the İzmir-Balıkesir Transfer Zone, western Anatolia. *J. Geodyn.* **2013**, *65*, 117–135. [CrossRef]

47. Duman, T.Y.; Çan, T.; Emre, Ö.; Kadirioğlu, F.T.; Başarır Baştürk, N.; Kılıç, T.; Arslan, S.; Özalp, S.; Kartal, R.F.; Kalafat, D.; et al. Seismotectonics database of Turkey. *Bull. Earthq. Eng.* **2018**, *16*, 3277–3316. [CrossRef]
48. Tan, O.; Tapirdamaz, M.C.; Yörük, A. The earthquakes catalogues for Turkey. *Turk. J. Earth Sci.* **2008**, *17*, 405–418.
49. Eyübagil, E.E.; Solak, H.İ.; Kavak, U.S.; Tiryakioglu, İ.; Sözbilir, H.; Aktuğ, B.; Özkaymak, Ç. Present day strike-slip deformation within the southern part of the İzmir-Balıkesir Transfer Zone based on GNSS data and implications for seismic hazard assessment in western Anatolia, Turk. *J. Earth Sci.* **2021**, *30*, 143–160.
50. Pavlides, S.; Caputo, R. Magnitude versus faults' surface parameters: Quantitative relationships from the Aegean Region. *Tectonophysics* **2004**, *380*, 159–188. [CrossRef]
51. Bozkurt, E.; Sozbilir, H. Evolution of the large-scale active manisa fault, Southwest Turkey: Implications on fault development and regional tectonics. *Geodin. Acta* **2006**, *19*, 427–453. [CrossRef]
52. Nicol, A.; Mouslopoulou, V.; Begg, J.; Oncken, O. Displacement accumulation and sampling of paleoearthquakes on active normal faults of Crete in the eastern Mediterranean. *Geochem. Geophys. Geosyst.* **2020**, *21*, e2020GC009265. [CrossRef]
53. United States Geological Survey National Earthquake Information Center. Available online: https://earthquake.usgs.gov/earthquakes/eventpage/us7000c7y0/executive (accessed on 26 October 2021).
54. McKenzie, D. Active tectonics of the Alpine-Himalayan belt: The Aegean Sea and surrounding regions. *Geophys. J. Int.* **1978**, *55*, 217–254. [CrossRef]
55. Ambraseys, N.N.; Jackson, J.A. Faulting associated with historical and recent earthquakes in the Eastern Mediterranean region. *Geophys. J. Int.* **1998**, *133*, 390–406. [CrossRef]
56. Bozkurt, E. Neotectonics of Turkey: A synthesis. *Geodin. Acta* **2001**, *14*, 3–30. [CrossRef]
57. Ambraseys, N.N. Engineering seismology. *Earthq. Eng. Struct. Dyn.* **1988**, *17*, 51–105. [CrossRef]
58. Guidoboni, E.; Comastri, A.; Triana, G. *Catalogue of Ancient Earthquakes in the Mediterranean Area up to the 10th Century*; Istituto Nazionale di Geofisica: Rome, Italy, 1994; ISBN 88-85213-06-5.
59. Özkaymak, Ç.; Sözbilir, H.; Uzel, B.; Akyüz, H.S. Geological and palaeoseismological evidence for Late Pleistocene-Holocene activity on the Manisa Fault Zone, western Anatolia. *Turk. J. Earth Sci.* **2011**, *20*, 449–474.
60. Özkaymak, Ç.; Sözbilir, H. Tectonic Geomorphology of the Spildağı High Ranges, Western Anatolia. *Geomorphology* **2012**, *173–174*, 128–140. [CrossRef]
61. Allen, C.R. Geological criteria for evaluating seismicity. *Geol. Soc. Am. Bull.* **1974**, *86*, 1041–1057. [CrossRef]
62. Paton, S. Active normal faulting, drainage patterns and sedimentation in southwestern Turkey. *J. Geol. Soc.* **1992**, *149*, 1031–1044. [CrossRef]
63. Hanson, K.L.; Kelson, K.I.; Angell, M.A.; Lettis, W.R. *Techniques for Identifying Faults and Determining Their Origins*; Contract Rep. NUREG/CR-5503; Nuclear Regulatory Commission: Washington, DC, USA, 1999; p. 504.
64. McCalpin, J.P. (Ed.) Paleoseismology. In *International Geophysics*, 2nd ed.; Academic Press: Cambridge, MA, USA, 2009; p. 629.
65. Yeats, R. Active Faults Related to Folding. In *Active Tectonics: Studies in Geophysics*; National Academy Press: Washington, DC, USA, 1986.
66. Ergin, K.; Güçlü, U.; Uz, Z. *A Catalogue of Earthquakes for Turkey and Surrounding Area (11 AD.-1964)*; Technical Report, no. 24; İstanbul Technical University: İstanbul, Turkey, 1967.
67. Ambraseys, N.N.; Finkel, C.F. *The Seismicity of Turkey and Adjacent Areas: A Historical Review, 1500–1800*; Eren Publishing & Book Trade: İstanbul, Turkey, 1995; p. 240.
68. Papazachos, B.; Papazachou, C. *The Earthquakes of Greece, Technical Books Edition*; Thessaloniki: Thessaloniki, Greece, 1997; p. 304.
69. Kandilli Observatory and Earthquake Research Institute. Boğaziçi University. Available online: http://www.koeri.boun.edu.tr/new/en (accessed on 26 October 2021).
70. Stone, J.O.; Allan, G.L.; Fifield, L.K.; Cresswell, R.G. Cosmogenic chlorine-36 from calcium spallation. *Geochim. Cosmochim. Acta* **1996**, *60*, 679–692. [CrossRef]
71. Ivy-Ochs, S.; Synal, H.A.; Roth, C.; Schaller, M. Initial results from isotope dilution for Cl and Cl-36 measurements at the PSI/ETH Zurich AMS facility. *Nucl. Instrum. Methods Phys. Res. Sect. B Beam Interact. Mater. At.* **2004**, *223–224*, 623–627. [CrossRef]
72. Ivy-Ochs, S.; Poschinger, A.V.; Synal, H.A.; Maisch, M. Surface exposure dating of the Flims landslide, Graubunden, Switzerland. *Geomorphology* **2009**, *103*, 104–112. [CrossRef]
73. Elmore, D.; Ma, X.; Miller, T.; Mueller, K.; Perry, M.; Rickey, F.; Sharma, P.; Simms, P.; Lipschutz, M.; Vogt, S. Status and plans for the PRIME Lab AMS facility. *Nucl. Instrum. Methods Phys. Res. Sect. B Beam Interact. Mater. At.* **1997**, *123*, 69–72. [CrossRef]
74. Evans, J.M.; Stone, J.O.H.; Fifield, L.K.; Cresswell, R.G. Cosmogenic chlorine-36 production in K-feldspar. *Nucl. Instrum. Methods Phys. Res. Sect. B Beam Interact. Mater. At.* **1997**, *123*, 334–340. [CrossRef]
75. Fink, D.; Vogt, S.; Hotchkis, M. Cross-sections for Cl-36 from Ti at E-p=35–150 MeV: Applications to in-situ exposure dating. *Nucl. Instrum. Methods Phys. Res. Sect. B Beam Interact. Mater. At.* **2000**, *172*, 861–866. [CrossRef]
76. Stone, J.O. Terrestrial chlorine-36 production from spallation of iron. In Proceedings of the 10th International Conference on Accelerator Mass Spectrometry, Berkeley, CA, USA, 5–10 September 2005.
77. Alfimov, V.; Ivy-Ochs, S. How well do we understand production of Cl-36 in limestone and dolomite? *Quat. Geochronol.* **2009**, *4*, 462–474. [CrossRef]
78. Stone, J.O. Air pressure and cosmogenic isotope production. *J. Geophys. Res.* **2000**, *105*, 23753–23759. [CrossRef]

79. Heisinger, B.; Lal, D.; Jull, A.J.T.; Kubik, P.; Ivy-Ochs, S.; Neumaier, S.; Knie, K.; Lazarev, V.; Nolte, E. Production of selected cosmogenic radionuclides by muons: 1. Fast muons. *Earth Planet. Sci. Lett.* **2002**, *200*, 345–355. [CrossRef]
80. Heisinger, B.; Lal, D.; Jull, A.J.T.; Kubik, P.; Ivy-Ochs, S.; Knie, K.; Nolte, E. Production of selected cosmogenic radionuclides by muons: 2. Capture of negative muons. *Earth Planet. Sci. Lett.* **2002**, *200*, 357–369. [CrossRef]
81. Wells, D.L.; Coppersmith, J.K. New empirical relationships among magnitude, rupture length, rupture width, rupture area, and surface displacement. *Bull. Seismol. Soc. Am.* **1994**, *84*, 974–1002.
82. Wesnousky, S.G. Displacement and Geometrical Characteristics of Earthquake Surface Ruptures: Issues and Implications for Seismic-Hazard Analysis and the Process of Earthquake Rupture. *Bull. Seismol. Soc. Am.* **2008**, *98*, 1609. [CrossRef]
83. Walsh, J.J.; Watterson, J. Analysis of the relationship between the displacements and dimensions of faults. *J. Struct. Geol.* **1988**, *10*, 239–247. [CrossRef]
84. Marrett, R.; Allmendinger, R.W. Estimates of strain due to brittle faulting: Sampling of fault populations. *J. Struct. Geol.* **1991**, *13*, 735–738. [CrossRef]
85. Kim, Y.S.; Sanderson, D.J. The relationship between displacement and length of faults: A review. *Earth-Sci. Rev.* **2005**, *68*, 317–334. [CrossRef]
86. Perrey, A. Note sur les tremblements de terre ressentis en 1847. *Mem. Acad. Sci. Arts Belles-Lett.* **1848**, *1847–1848*, 68–115.
87. Denton, G.H.; Anderson, R.F.; Toggweiler, J.R.; Edwards, R.L.; Schaefer, J.M.; Putnam, A.E. The Last Glacial Termination. *Science* **2010**, *328*, 1652–1656. [CrossRef] [PubMed]
88. Shakun, J.D.; Carlson, A.E. A global perspective on Last Glacial Maximum to Holocene climate change. *Quat. Sci. Rev.* **2010**, *29*, 1801–1816. [CrossRef]
89. Stern, J.V.; Lisiecki, L.E. Termination 1 timing in radiocarbon-dated regional benthic δ18O stacks. *Paleoceanography* **2014**, *29*, 1127–1142. [CrossRef]